USGS
science for a changing world

هيئة المساحة الجيولوجية السعودية
SAUDI GEOLOGICAL SURVEY

Isotopic and Geochemical Evidence for the Source of Volcanism at Harrat Rahat, Kingdom of Saudi Arabia

Chapter J of
Active Volcanism on the Arabian Shield—Geology, Volcanology, and Geophysics of Northern Harrat Rahat and Vicinity, Kingdom of Saudi Arabia

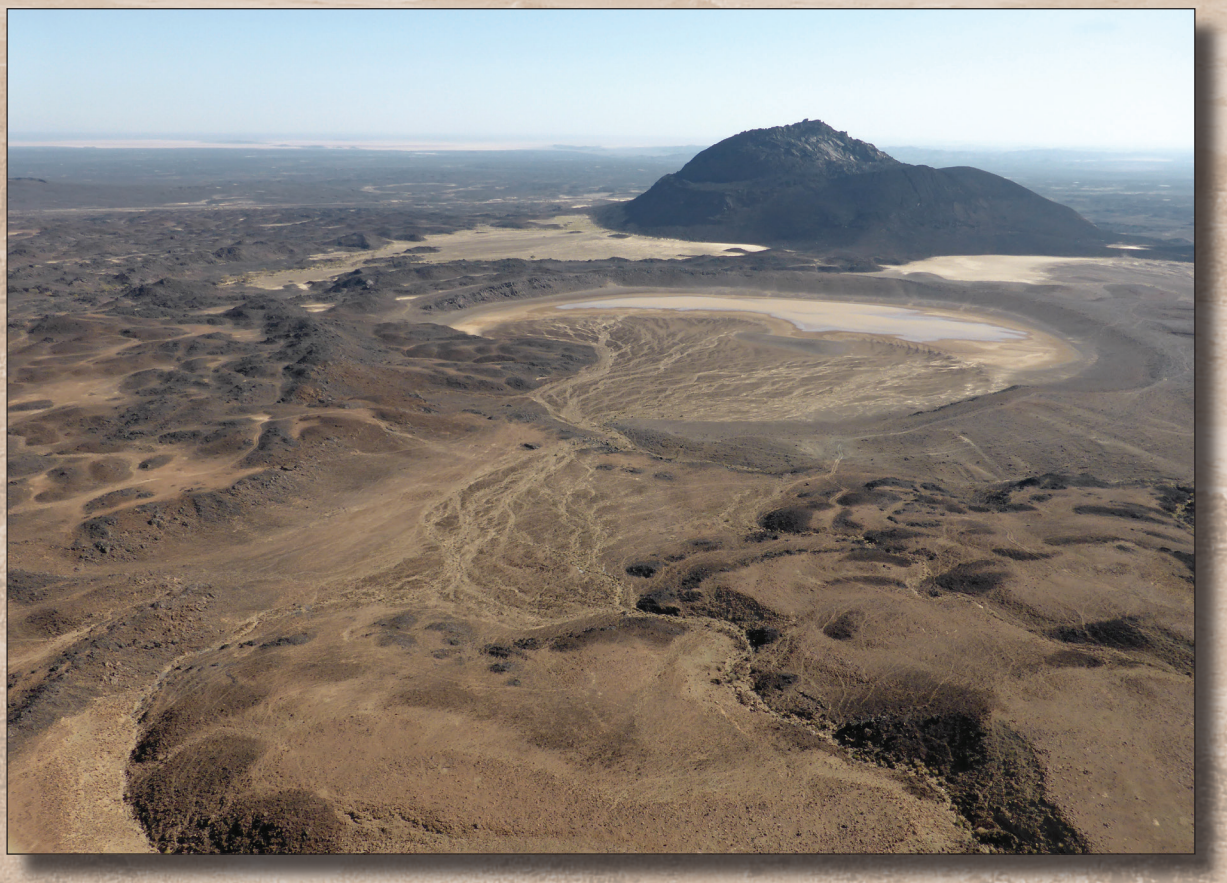

U.S. Geological Survey Professional Paper 1862
Saudi Geological Survey Special Report SGS–SP–2021–1

U.S. Department of the Interior
U.S. Geological Survey

Cover. Aerial view east across the basaltic maar crater of Gura 1 with the trachyte lava dome of Dabaa 1 in the background. The Gura 1 maar is about 0.7 kilometers (km) across, rim to rim, and is overridden by mugearite lava on the north (left) and east (lower foreground) with its characteristic lumpy or mounded surface. The Dabaa 1 trachyte dome is about 1 km across and stands as much as 220 meters above the surroundings. U.S. Geological Survey photograph by T.W. Sisson, February 12, 2014. Background image shows northern Harrat Rahat lava flows, maars, and lava domes. U.S. Geological Survey photograph by Andrew Calvert, January 25, 2012.

Isotopic and Geochemical Evidence for the Source of Volcanism at Harrat Rahat, Kingdom of Saudi Arabia

By Vincent J.M. Salters, Afi Sachi-Kocher, Drew T. Downs, Mark E. Stelten, and Thomas W. Sisson

Chapter J of

Active Volcanism on the Arabian Shield—Geology, Volcanology, and Geophysics of Northern Harrat Rahat and Vicinity, Kingdom of Saudi Arabia

Edited by Thomas W. Sisson, Andrew T. Calvert, and Walter D. Mooney

U.S. Geological Survey Professional Paper 1862
Saudi Geological Survey Special Report SGS–SP–2021–1

U.S. Department of the Interior
U.S. Geological Survey

U.S. Geological Survey, Reston, Virginia: 2023

For more information on the USGS—the Federal source for science about the Earth, its natural and living resources, natural hazards, and the environment—visit https://www.usgs.gov or call 1–888–ASK–USGS.

For an overview of USGS information products, including maps, imagery, and publications, visit https://store.usgs.gov.

Suggested citation:
Salters, V.J.M., Sachi-Kocher, A., Downs, D.T., Stelten, M.E., and Sisson, T.W., 2023, Isotopic and geochemical evidence for the source of volcanism at Harrat Rahat, Kingdom of Saudi Arabia, chap. J *of* Sisson, T.W., Calvert, A.T., and Mooney, W.D., eds., Active volcanism on the Arabian Shield—Geology, volcanology, and geophysics of northern Harrat Rahat and vicinity, Kingdom of Saudi Arabia: U.S. Geological Survey Professional Paper 1862 [also released as Saudi Geological Survey Special Report SGS–SP–2021–1], 30 p., https://doi.org/10.3133/pp1862J.

Associated data for this publication:
Salters, V.J.M., and Sisson, T.W., 2023, Isotopic compositions (Sr, Nd, Hf, Pb) of Quaternary volcanic rocks of northern Harrat Rahat, Kingdom of Saudi Arabia: U.S. Geological Survey data release, https://doi.org/10.5066/P9FOBQNK.

ISSN 1044-9612 (print)
ISSN 2330-7102 (online)

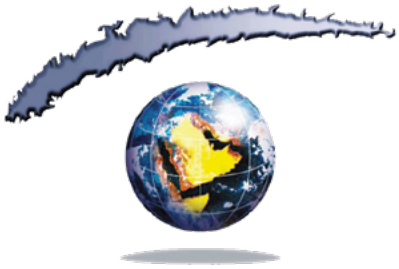

هيئة المساحة الجيولوجية السعودية
SAUDI GEOLOGICAL SURVEY

Ministry of Industry and Mineral Resources
BANDAR BIN IBRAHIM BIN ABDULLAH AL-KHORAYEF, Minister and SGS Chairman

Saudi Geological Survey
Abdullah bin Mufter Al-Shamrani, Chief Executive Officer

Saudi Geological Survey, Jiddah, Kingdom of Saudi Arabia: 2023

Contents

Figures

Tables

Abbreviations

BSE	bulk silicate earth
°C	degrees Celsius
CHUR	chondritic uniform reservoir
D	bulk partition coefficient
DM	depleted mantle
E&A	Eimer and Amend
fO_2	oxygen fugacity
GPa	gigapascal
km	kilometer
Ma	mega-annum
Mg#	Mg number; Mg# = Mg/[Mg+Fe^{2+}], molar
MORB	midocean ridge basalt
NHRL	Northern Hemisphere Reference Line
ppm	parts per million, by weight
REE	rare earth element
TIMS	thermal ionization mass spectrometry

Active Volcanism on the Arabian Shield
Edited by T.W. Sisson, A.T. Calvert, and W.D. Mooney
U.S. Geological Survey Professional Paper 1862
Saudi Geological Survey Special Report SGS–SP–2021–1

Chapter J

Isotopic and Geochemical Evidence for the Source of Volcanism at Harrat Rahat, Kingdom of Saudi Arabia

By Vincent J.M. Salters,[1] Afi Sachi-Kocher,[1] Drew T. Downs,[2] Mark E. Stelten,[2] and Thomas W. Sisson[2]

Abstract

Pleistocene and Holocene basalts, hawaiites, mugearites, benmoreites, and trachytes from the northern part of the Harrat Rahat volcanic field, Kingdom of Saudi Arabia, were analyzed for Sr, Nd, Hf, and Pb isotopic compositions. Evolved trachytes with Mg number <0.1 (Mg# = Mg/[Mg+Fe^{2+}], molar) have relatively radiogenic Sr isotopic compositions indicating that they were influenced by contamination probably in the upper crust. Volcanic rocks with Mg# >0.1, consisting chiefly of alkali basalts but encompassing hawaiites, mugearites, and benmoreites, show a limited range in Hf, Nd, Sr, and Pb isotopic compositions. Although the total Pb isotope variation is only 1 percent, the Pb isotope values correlate with Mg#, where the least radiogenic Pb is in samples with the lowest Mg#. The trend formed in Pb isotope space points toward an unradiogenic Pb composition that is similar to the Pb isotopic composition of lower crust of the Precambrian Arabian-Nubian Shields, as well as to feldspars and galena in the upper crust of the western Arabian Shield. This trend is interpreted as progressive but overall minor (no more than 5 weight percent) assimilation of shield rocks, or their partial melts, during fractional crystallization.

Isotopic compositions of the least evolved northern Harrat Rahat magmas are most similar among analyzed Arabian harrats to depleted spreading-ridge basalts of the active Red Sea rift, but isotopic values are displaced toward those of spreading-ridge basalts of the Gulf of Aden that are proximal to the site of the Afar mantle plume. The Pb isotopic compositions very near the Northern Hemisphere Reference Line indicate no discernable lithospheric contribution to yield the parental basalts of northern Harrat Rahat, and their isotopic compositions are consistent with derivation predominantly from depleted Northern Hemisphere asthenosphere with a subordinate (20–30 weight percent) component from the Afar mantle plume.

Trace-element variations show that appreciable portions of melting were in the garnet stability field, confirming the sub-lithospheric origin of the magmas, and that melting extents were low, accounting for the alkalic, trace-element-enriched character of the suite. The presence of possible Afar mantle beneath the western part of the Arabian Shield and its absence beneath the Red Sea rift may result from capture and channelized flow along high-relief structures incised into the base of the sub-continental lithosphere, as revealed by geophysical images.

Introduction

The Harrat Rahat volcanic field is part of the Cenozoic Arabian volcanic province, a northwest-southeast-trending belt of volcanic fields on the western side of the Arabian Peninsula that extends from the Gulf of Aden at the peninsula's southern end north to the Mediterranean Sea (fig. 1). It is 25° oblique to and offset from the Red Sea rift. Most of the volcanism in this province is less than 10 million years in age (Ma). The dominantly basaltic magmas erupted on the stable Precambrian Arabian continental shield that ranges in age from 900–700 Ma (Stoeser and Frost, 2006). The crust of the Arabian volcanic province is uplifted, possibly caused by thinning of the mantle lithosphere under the province (Camp and Roobol, 1992; Chang and others, 2011; Yao and others, 2017).

There have been several geochemical studies of volcanic fields within the Arabian volcanic province, each known in Arabic as a harrat (حَرَّة) Camp and Roobol (1989, 1991) and Camp and others (1987, 1991, 1992) reported on five of the harrats in the Kingdom of Saudi Arabia. Those and other studies recognized three general phases of Cenozoic magmatism. The first commenced near 31 Ma, before opening of the Red Sea and Gulf of Aden, and produced the voluminous basaltic traps of Yemen, Ethiopia, and Sudan, collectively interpreted as melting products of the head of the Afar mantle plume. This was followed at about 23–22 Ma in Arabia by a period of extensive tholeiitic basaltic diking and localized volcanism adjacent and parallel to the Red Sea that records its initial rifting. These first and second phases of magmatism in the Arabian volcanic province may not have been separated by a hiatus, but the locus and style of magmatism differed. The currently active harrat volcanism commenced near 14 Ma coincident with uplift of the Ḥijāz and ʻAsīr highlands, initiation of Aqaba-Dead Sea transform faulting, and possibly, commencement of organized seafloor spreading in the Red Sea (Coleman and others, 1983;

[1]Florida State University.

[2]U.S. Geological Survey.

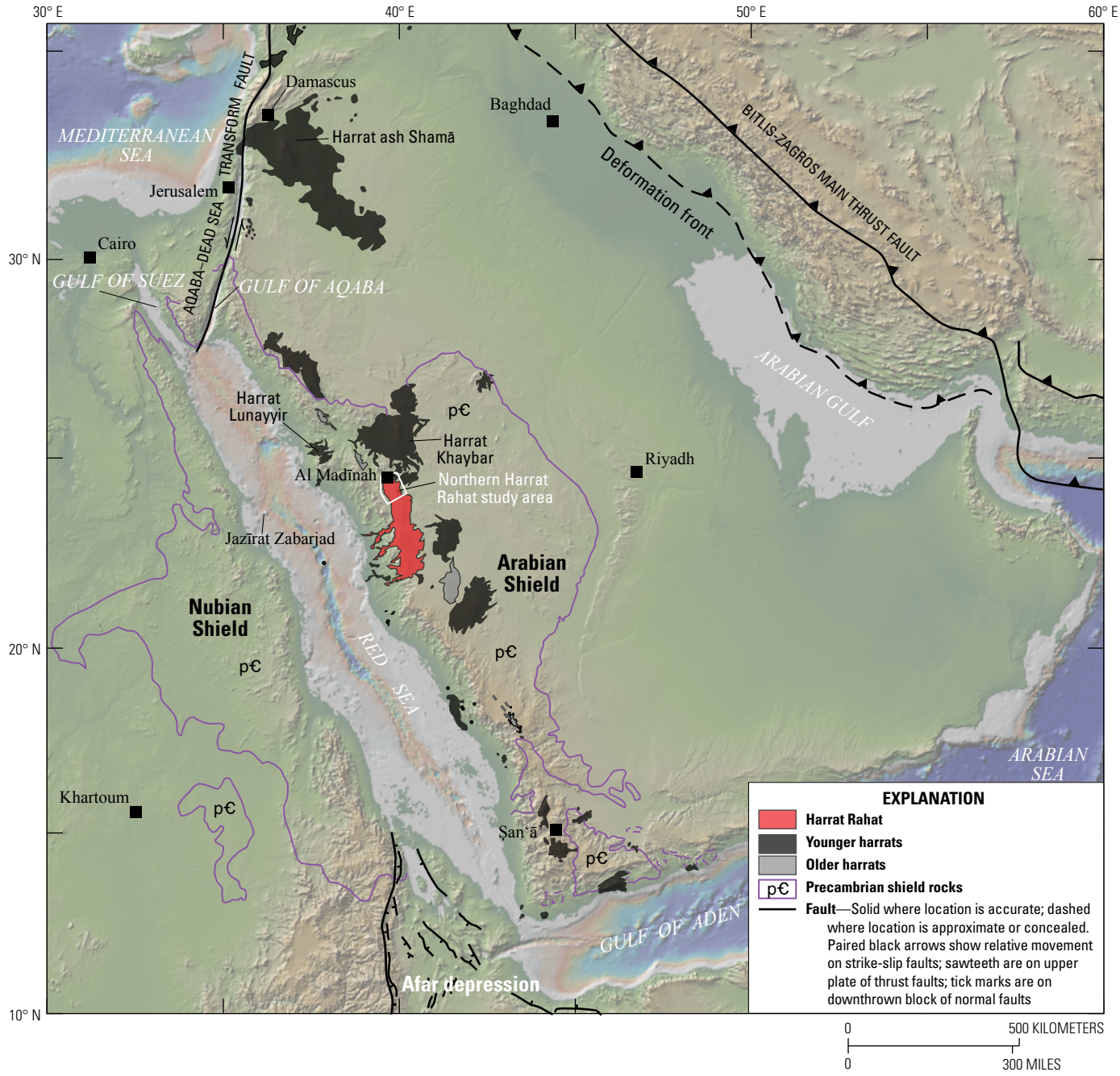

Figure 1. Colored shaded-relief map of the Arabia Plate and vicinity showing harrats of the Cenozoic Arabian volcanic province. The study area is outlined in white. Harrats mainly younger than 14 million years old are shown in dark gray and those with abundant Oligocene or early Miocene rocks are shown in light gray. Not shown are Oligocene traps of Yemen, near Ṣan'ā', and all Cenozoic volcanic rocks of the greater Afar area. Shaded-relief base map generated with GeoMapApp using global multiresolution topography and bathymetry (Ryan and others, 2009). Vertical exaggeration is 8×; map uses Mercator projection.

Bohannon and others, 1989; Coleman, 1993; Bosworth, 2015; Reilinger and others, 2015; Calvert and Sisson, 2023). This youngest phase of shield volcanism is consistently alkalic and is enriched in large ion lithophile elements.

Camp and Roobol (1992) argued that recent harrat volcanism of Saudi Arabia is the combined product of a deep active upwelling component, such as a plume, and a shallow component similar to that fueling spreading-ridge volcanism in the Gulf of Aden, such as ambient asthenospheric upper mantle. Moufti and others (2012) interpreted, based on trace-element and isotopic compositions, that the mantle source of northern Harrat Rahat (referred to by those authors as Harrat al Madīnah) has both asthenospheric and lithospheric components, and that the alignment of the volcanoes indicates strong lithospheric control. The authors also argue for the presence of amphibole in the source on the basis of relatively

high concentrations of Ba, Nb, and Th. A recent study of Harrat Lunayyir and Harrat Khaybar (Sanfilippo and others, 2019) came to similar conclusions as Moufti and others (2012), whereas Duncan and Al-Amri (2013) interpreted Harrat Lunayyir magmas as melting products of upwelling asthenosphere arrested at the base of the mantle lithosphere with no unambiguous contributions either from a compositionally distinct mantle plume or the lithospheric upper mantle. Altherr and others (1990) suggested that the harrat magmatism differs from Red Sea rift magmatism because of contamination of the Red Sea asthenosphere with lithospheric material. In a study of the Harrat ash Shamā volcanic field in Jordan, Shaw and others (2003) argue for melts derived both from the garnet and spinel stability fields and, on the basis of Pb isotopic compositions, that the mantle enrichment is unrelated to the Afar plume volcanism that is prominent in Yemen. Quaternary mafic volcanism near Ṣan‘ā’, Yemen, is part of the Arabian volcanic province; however, some argue that it is influenced by the Afar plume because it has higher $^{208}Pb/^{204}Pb$ for given $^{206}Pb/^{204}Pb$ values than harrat volcanic rocks in Saudi Arabia and Jordan (Baker and others, 1997). It must be noted that the composition proposed for the Afar plume is not constant throughout the literature, and the composition used by Baker and others (1997) is higher in $^{208}Pb/^{204}Pb$ than the more recently estimated composition by Rooney and others (2012).

Geodynamic models for recent volcanism in the Arabian volcanic province also differ. One model argues for fossil plume material accreted onto the base of the sub-continental lithosphere that is now passively melting by thinning and rifting (Altherr and others, 1990; Stein and Hofmann, 1992; Stein and Goldstein, 1996). Camp and Roobol (1992) argue for hot asthenosphere either rising as a plume or a lobe originating in the region of the Afar plume. Ebinger and Sleep (1998) argue that the plume head eroded the base of the lithosphere over a large area allowing plume material to be channelized under what is now the Arabian volcanic province. Chang and others (2011) and Yao and others (2017) image a belt of upper mantle with low seismic velocity incised through much of the mantle lithosphere, with the greatest thinning and lowest seismic velocities centered beneath the larger harrats of western Arabia, including Harrat Rahat, much as proposed by Ebinger and Sleep (1998), and argue for channelized northward flow of the mantle away from the Afar region. Sisson and others (2023) derive a mantle source composition and potential temperature for northern Harrat Rahat magmas similar in most respects to those inferred for the depleted asthenospheric sources that yield midocean ridge basalts (MORB), and propose that the harrat magmas derive predominantly from low-degree melting of such depleted asthenosphere, admixed with subordinate material either from the Afar plume or as enriched domains in the ambient asthenosphere. They further speculate that upwelling and partial melting are localized and continue beneath the harrat belt by a magmatic feedback mechanism that incises the base of the lithosphere.

One of the goals of this study is to determine the relation between Harrat Rahat magmas and the various proposed sources and melting mechanisms. The Harrat Rahat mantle source can potentially have kinship with Red Sea rift basalts, the Afar plume, Indian Ocean-type asthenosphere, and sub-continental lithosphere of the Arabian Shield. Associations with the different potential sources have consequences for interpretations of mantle flow and the geodynamic models for the origin for the Harrat Rahat basalts. The high-precision radiogenic isotope compositions in combination with major- and trace-element concentrations help test the models.

Sample Suite

Samples analyzed for isotopic composition were collected in the course of detailed geologic mapping and associated investigations of eruptive style, history, and hazards of the northern part of Harrat Rahat spanning from the city of Al Madīnah al Munawwarah south about 70 kilometers (km). Volcanic rocks that make up the exposed surface of the study area, investigated herein isotopically, mainly erupted over the last 350,000 years, although volcanic rocks as old as 1.2 Ma have been identified in the study area (Stelten and others, 2020, 2023), and the inception of volcanism for greater Harrat Rahat is estimated at about 10 Ma (Camp and Roobol, 1991). The great majority of the study area consists of alkali basalt lava flows with subordinate hawaiites, and with more evolved mugearites, benmoreites, and trachytes collectively making up about 15 percent of the volcanic products in approximately equal abundances. Few basalts are weakly hypersthene normative and are referred to as transitional, although they lack modal low-calcium pyroxene and are mineralogically and texturally indistinguishable from the nepheline-normative alkali basalts (Camp and Roobol, 1991; Sisson and others, 2023). Downs (2019) reports major-oxide and trace-element compositions of volcanic rocks from northern Harrat Rahat, including all those employed in this study; additional chemical analyses of Harrat Rahat volcanic rocks are reported by Coleman and others (1983), Moufti (1985), Camp and others (1987), Camp and Roobol (1989, 1991), Moufti and others (2012), and Murcia and others (2016). For convenience of the reader, the major-oxide and trace-element concentrations of the samples analyzed for isotopic composition are presented in tables 1 and 2, classified following Cox and others (1979) with ferric and ferrous iron recalculated as appropriate for melts at the oxygen fugacity of the quartz-fayalite-magnetite assemblage (Sisson and others, 2023). Basalts are typified by sparse phenocrysts of olivine and plagioclase, although geochemical relations indicate co-crystallization of clinopyroxene that is absent as a phenocryst (Sisson and others, 2023). Hawaiites generally are distinguished by the additional presence of titanomagnetite microphenocrysts, and mugearites by the additional presence of clinopyroxene and apatite microphenocrysts. Some benmoreites and all trachytes have a phenocryst assemblage consisting almost entirely of alkali feldspar, accompanied by trace microphenocrysts of sodic clinopyroxene, titanomagnetite, apatite, and in some samples, fayalite. A total of 70 rocks were analyzed for isotopic composition, consisting of 31 alkali basalts, 2 transitional basalts, 9 hawaiites, 8 mugearites, 7 benmoreites, and 13 trachytes.

Table 1. Locations and major-oxide concentrations, in normalized weight percent, of northern Harrat Rahat volcanic rocks analyzed for isotopic composition.

[Eastings and northings in meters for Universal Transverse Mercator zone 37R using the World Geodetic System 1984 datum. Major-oxide analyses by X-ray fluorescence recalculated from Downs (2019) by normalizing to 100 weight percent totals with Fe_2O_3 and FeO as appropriate for melts at the quartz-fayalite-magnetite oxygen buffer (from Sisson and others, 2023). Total gives original major-oxide total with all Fe as FeO. Rock types are classified as in Cox and others (1979); Hy and Qtz indicate CIPW normative hypersthene and quartz; all other samples are nepheline normative. Trans., transitional; Mg# = Mg/[Mg+Fe^{2+}], molar]

Sample	Type	Easting	Northing	SiO_2	TiO_2	Al_2O_3	Fe_2O_3	FeO	MnO	MgO	CaO	Na_2O	K_2O	P_2O_5	Total	Mg#
R14AC052	Trans. basalt (Hy)	590179	2655647	47.8	1.60	15.9	1.88	9.71	0.17	8.74	11.0	2.71	0.39	0.16	99.43	0.616
R14AC088	Trans. basalt (Hy)	589261	2677501	47.2	2.11	16.6	2.04	10.5	0.18	7.93	9.47	3.04	0.63	0.31	97.25	0.574
R15DS124	Alkali basalt	581090	2665987	47.6	1.48	16.6	1.74	9.00	0.17	8.52	11.9	2.53	0.30	0.14	98.89	0.628
R14AC022	Alkali basalt	592479	2679699	47.5	1.96	15.3	2.04	10.4	0.19	9.67	8.27	3.50	0.78	0.42	98.85	0.624
R14TS001	Alkali basalt	586207	2679784	47.2	1.86	16.2	1.88	9.65	0.17	8.93	10.3	3.09	0.41	0.22	99.38	0.623
R15TS184	Alkali basalt	577062	2672965	47.6	1.55	16.6	1.80	9.33	0.17	8.12	11.5	2.73	0.32	0.17	99.67	0.608
R14TS026[a]	Alkali basalt	600012	2697759	46.0	2.47	16.2	1.92	9.88	0.21	8.46	11.2	2.84	0.53	0.36	99.21	0.604
R15DS105	Alkali basalt	595916	2690209	46.1	2.33	15.8	2.01	10.4	0.18	8.74	11.0	2.80	0.43	0.23	99.62	0.600
R15MS031	Alkali basalt	589420	2699949	46.5	1.92	15.8	2.06	10.6	0.19	8.79	10.0	3.17	0.54	0.36	99.28	0.596
R14AC018	Alkali basalt	592242	2679233	48.4	1.99	16.0	1.90	9.54	0.18	7.70	9.12	3.84	0.98	0.39	99.25	0.590
R15DD051	Alkali basalt	578923	2667891	48.0	2.01	16.0	2.02	10.2	0.19	8.13	8.47	3.68	0.89	0.48	98.85	0.587
R15DS174	Alkali basalt	603762	2664722	47.5	1.89	16.4	2.00	10.2	0.20	7.60	10.10	3.25	0.62	0.32	100.33	0.570
R14DS053	Alkali basalt	589500	2664469	46.9	2.45	15.9	2.10	10.7	0.20	7.74	9.23	3.48	0.76	0.50	99.48	0.563
R15DD145	Alkali basalt	572740	2679533	46.1	2.81	16.1	2.09	10.6	0.19	7.36	10.1	3.52	0.70	0.42	99.64	0.553
R15MS021	Alkali basalt	569465	2675983	47.1	2.27	16.1	2.12	10.8	0.20	7.30	9.65	3.46	0.62	0.39	99.42	0.546
R14AC009	Alkali basalt	586015	2691406	45.2	3.48	15.8	2.21	11.2	0.18	7.49	9.70	3.68	0.77	0.33	99.12	0.544
R14TS033	Alkali basalt	584610	2681045	45.5	3.49	16.1	2.21	11.1	0.19	7.13	8.90	3.81	1.01	0.55	99.56	0.534
R14AC066	Alkali basalt	601665	2671983	47.9	2.43	16.5	2.05	10.3	0.20	6.28	8.93	4.03	0.89	0.51	99.83	0.521
R14AC084	Alkali basalt	592366	2671105	46.0	2.66	15.5	2.25	11.4	0.21	6.99	9.86	3.57	0.72	0.80	99.64	0.522
R14TS014[a]	Alkali basalt	584857	2703739	44.5	3.47	16.0	2.12	10.7	0.20	6.47	11.7	3.63	0.83	0.40	96.56	0.519
R15DS097	Alkali basalt	580618	2701714	45.8	3.73	16.5	2.21	11.2	0.21	6.56	9.02	3.52	0.81	0.44	99.32	0.511
R16MS057	Alkali basalt	584487	2658457	46.5	3.06	16.4	2.23	11.3	0.20	6.52	8.87	3.56	0.77	0.55	99.89	0.507
R15TS169	Alkali basalt	569252	2686959	48.1	2.28	16.4	2.09	10.4	0.20	5.93	8.64	4.17	1.15	0.63	99.62	0.504
R15TS191	Alkali basalt	568962	2671123	46.4	3.22	16.5	2.22	11.1	0.20	6.37	8.67	3.87	0.88	0.54	99.49	0.506
R14AC069	Alkali basalt	590358	2681448	46.5	3.18	16.6	2.16	10.8	0.20	6.15	9.01	4.00	0.93	0.49	99.71	0.504
R14AC068	Alkali basalt	596910	2677863	47.9	2.54	16.9	2.09	10.4	0.20	5.89	8.51	4.19	0.93	0.43	99.88	0.502
R15MS029	Alkali basalt	587097	2695017	47.5	2.38	16.4	2.15	10.6	0.22	6.02	8.35	4.40	1.13	0.86	99.85	0.503
R14DS020	Alkali basalt	567624	2689103	46.9	2.69	16.4	2.17	10.8	0.22	5.87	8.86	4.11	0.96	0.94	99.73	0.492
R14AC058[a]	Alkali basalt	580868	2680708	46.1	3.66	16.6	2.34	11.7	0.22	5.47	8.10	3.91	1.02	0.83	99.56	0.455
R15TS197	Alkali basalt	560403	2669086	46.2	3.27	16.9	2.23	11.2	0.20	5.96	8.78	3.97	0.86	0.52	99.26	0.487
R15TS202	Alkali basalt	593341	2676141	48.3	2.18	16.4	2.12	10.6	0.21	5.50	8.89	4.05	1.05	0.73	99.58	0.480
R15DD047	Alkali basalt	575967	2667416	46.7	3.14	17.0	2.22	11.2	0.20	5.56	8.70	3.75	0.85	0.66	99.61	0.469
R14TS079	Alkali basalt	586264	2677112	48.0	2.52	16.8	2.18	10.8	0.21	5.16	8.29	4.34	1.18	0.58	99.68	0.460
R14TS018	Hawaiite	583252	2697945	48.2	2.39	16.4	2.09	10.2	0.22	5.45	8.32	4.45	1.38	0.88	99.13	0.488
R14TRO133	Hawaiite	572287	2690493	48.1	2.44	16.4	2.22	10.8	0.23	4.89	7.59	4.83	1.32	1.23	99.50	0.447
R15MS017	Hawaiite	591577	2688452	50.0	2.12	16.9	2.10	10.2	0.24	4.31	7.43	4.64	1.52	0.62	99.35	0.430
R15MS022	Hawaiite	570114	2676455	46.9	3.33	16.2	2.29	11.2	0.23	4.71	8.41	4.57	1.19	0.95	99.08	0.428
R14AC101	Hawaiite	569852	2699714	47.1	2.70	16.3	2.33	11.3	0.24	4.69	7.71	4.98	1.34	1.39	100.00	0.425
R15TS162	Hawaiite	576251	2688448	47.3	2.66	16.2	2.33	11.2	0.25	4.31	7.58	5.04	1.47	1.60	99.63	0.407
R14AC072	Hawaiite	595357	2663246	47.6	3.26	16.4	2.31	11.1	0.22	4.27	7.47	5.03	1.38	0.97	99.47	0.407

Table 1. Locations and major-oxide concentrations, in normalized weight percent, of northern Harrat Rahat volcanic rocks analyzed for isotopic composition.—Continued

Sample	Type	Easting	Northing	SiO_2	TiO_2	Al_2O_3	Fe_2O_3	FeO	MnO	MgO	CaO	Na_2O	K_2O	P_2O_5	Total	Mg#
R15DS156	Hawaiite	588695	2681941	48.2	2.94	16.2	2.44	11.9	0.25	4.10	7.17	4.56	1.49	0.82	99.05	0.380
R15MS008	Hawaiite	587182	2676149	47.6	2.58	15.8	2.59	12.4	0.27	3.76	6.97	5.03	1.56	1.40	99.43	0.351
R14DS003	Mugearite	585842	2685818	48.0	2.57	16.3	2.36	11.1	0.26	3.72	6.75	5.43	1.73	1.77	99.49	0.374
R14AC002	Mugearite	586035	2679566	49.9	2.27	16.3	2.22	10.2	0.25	3.23	6.26	5.72	2.09	1.59	99.95	0.361
R14TS037	Mugearite	585894	2680960	50.5	2.11	16.4	2.20	10.0	0.24	3.01	6.02	5.79	2.28	1.49	99.60	0.349
R14AC095	Mugearite	589223	2670228	50.8	2.03	16.7	2.26	10.4	0.24	2.77	6.10	5.52	2.20	1.01	99.54	0.322
R14AC048	Mugearite	591711	2670200	52.2	1.69	16.6	2.19	10.0	0.28	2.37	5.69	5.53	2.29	1.20	98.33	0.297
R14AC096	Mugearite	588989	2672786	51.9	1.69	16.8	2.20	10.0	0.26	2.33	5.49	6.04	2.11	1.21	99.79	0.293
R14AC021	Mugearite	591693	2679691	54.7	1.45	17.0	1.91	8.41	0.23	1.90	4.78	6.16	2.69	0.84	98.90	0.287
R16DD270	Mugearite (Hy)	594648	2665445	55.4	1.27	17.1	1.92	8.54	0.26	1.66	4.52	5.50	3.11	0.74	98.50	0.257
R14AC019	Benmoreite	592238	2679266	55.3	1.33	17.1	1.80	7.79	0.22	1.72	4.59	6.46	2.88	0.77	98.90	0.282
R14AC090	Benmoreite	590214	2677944	56.5	1.20	17.3	1.70	7.36	0.21	1.50	4.12	6.17	3.18	0.67	99.40	0.266
R14AC027	Benmoreite	597282	2666653	55.1	1.26	16.9	1.99	8.51	0.26	1.50	4.08	6.61	3.04	0.73	100.00	0.239
R14AC013	Benmoreite	590399	2675875	59.1	0.86	16.6	1.66	6.83	0.25	0.82	3.01	6.44	3.99	0.42	99.93	0.176
R14AC003	Benmoreite	588825	2675913	57.5	0.74	17.4	1.81	7.53	0.25	0.84	3.31	6.89	3.32	0.43	99.80	0.166
R14AC081	Benmoreite	594714	2666700	57.6	0.66	17.6	1.78	7.49	0.25	0.77	3.48	7.02	2.93	0.45	99.11	0.155
R14AC082	Benmoreite	594965	2667022	58.5	0.65	17.3	1.67	6.79	0.24	0.66	3.09	7.12	3.65	0.32	99.30	0.148
R15MS010	Trachyte	588560	2675414	63.2	0.04	17.6	0.71	2.77	0.19	0.34	3.48	7.02	4.66	0.01	95.51	0.179
R14TS070	Trachyte	590357	2676968	60.3	0.67	16.4	1.58	6.31	0.25	0.53	2.60	6.45	4.68	0.26	99.15	0.130
R14TRO050	Trachyte	592921	2665149	61.4	0.28	17.7	1.20	4.66	0.19	0.35	2.36	6.59	5.15	0.09	97.84	0.118
R14AC046	Trachyte	590130	2670847	59.9	0.45	17.1	1.63	6.64	0.27	0.49	2.61	6.50	4.20	0.20	98.63	0.116
R14AC010[a]	Trachyte	589155	2676995	61.1	0.11	17.2	1.02	3.84	0.19	0.18	3.99	7.30	4.97	0.04	96.38	0.077
R14AC070	Trachyte	595306	2662928	63.3	0.12	17.8	0.99	3.58	0.18	0.12	0.80	7.99	5.12	0.03	98.93	0.056
R14AC025	Trachyte	596742	2666166	64.7	0.06	17.1	0.86	3.15	0.19	0.07	1.02	8.12	4.71	0.02	97.23	0.038
R14TS068	Trachyte	585375	2679376	62.9	0.12	17.4	1.04	3.78	0.18	0.06	1.52	7.85	5.05	0.03	98.83	0.028
R14TRO038	Trachyte	597700	2664563	62.9	0.21	17.1	1.17	4.26	0.18	0.04	1.17	7.67	5.25	0.05	99.69	0.016
R14TS028	Trachyte	586169	2678421	62.9	0.11	17.1	1.13	3.96	0.19	0.03	0.93	8.71	4.92	0.02	99.28	0.013
R14AC051	Trachyte	590154	2655719	63.1	0.14	17.3	1.10	3.95	0.18	0.02	0.96	8.03	5.14	0.03	98.88	0.009
R14AC035	Trachyte (Hy)	593636	2665094	65.0	0.05	17.2	0.87	3.14	0.19	0.01	0.48	8.24	4.76	0.02	97.90	0.006
R14AC016	Trachyte (Hy, Qtz)	592186	2679424	64.5	0.15	15.1	1.28	4.59	0.25	0.07	0.70	8.62	4.62	0.05	97.50	0.026

[a]Sample has anomalously high CaO/Al_2O_3 or Cs/Rb, indicative of residual secondary minerals in the split analyzed for chemical composition.

Analytical Techniques

Isotopic compositions were analyzed on approximately 100 milligram splits of rock powder subjected to cold leaching with 2.5 normal HCl for 60 minutes. The leached fraction was rinsed several times using 18 megohm deionized water and then quartz-distilled water and finally dissolved in a 3:1 mixture of $HF:HNO_3$ using standard techniques. Pb, Hf, Sr, and Nd were separated from the same aliquot following the techniques outlined by Stracke and others (2003). Sr isotope ratios were measured by thermal ionization mass spectrometry (TIMS) on a Finnigan MAT 262 RPQ mass spectrometer in dynamic mode. $^{87}Sr/^{86}Sr$ ratios are corrected for fractionation to $^{86}Sr/^{88}Sr = 0.1194$. The long-term average for measurements of the Eimer and Amend (E&A) Sr standard yields a value of 0.708004±18 parts per million (ppm) (for n=50 measurements with an uncertainty of 2 standard deviations [2σ]). $^{87}Sr/^{86}Sr$ of the samples are reported relative to the accepted ratio of the E&A standard ($^{87}Sr/^{86}Sr = 0.70800$). Nd, Pb, and Hf isotope ratios were measured via multicollector inductively coupled plasma mass spectrometry on a ThermoFinnigan Neptune MC-ICP-MS. Pb-isotope ratios are normalized to the values for standard NBS981. Reproducibility of the standard is <50 ppm for $^{206}Pb/^{204}Pb$, <75 ppm for $^{207}Pb/^{204}Pb$, and <200 ppm for $^{208}Pb/^{204}Pb$. $^{143}Nd/^{144}Nd$ ratios are corrected for fractionation to $^{146}Nd/^{144}Nd = 0.7219$. $^{176}Hf/^{177}Hf$ ratios

Table 2. Trace-element concentrations, in parts per million by weight, of northern Harrat Rahat volcanic rocks analyzed for isotopic composition.

[Trace element concentrations from Downs (2019); rock types are classified as in Cox and others (1979); Hy and Qtz indicate CIPW normative hypersthene and quartz; all other samples are nepheline normative. Trans., transitional]

Sample	Type	Cs	Rb	Ba	Sr	Pb	Th	U	Zr	Hf	Nb	Ta	La
R14AC052	Trans. basalt (Hy)	0.051	4.56	69.2	316	0.773	0.552	0.257	99.6	2.43	8.03	0.66	8.17
R14AC088	Trans. basalt (Hy)	0.071	5.20	114	445	1.38	0.970	0.294	156	3.63	14.8	1.14	13.8
R15DS124	Alkali basalt	0.010	2.58	56.1	333	0.673	0.517	0.149	92.3	2.28	9.41	0.63	7.02
R14AC022	Alkali basalt	0.051	7.44	91.9	418	1.55	1.33	0.469	228	4.94	18.4	1.26	18.3
R14TS001	Alkali basalt	0.021	3.26	51.3	419	0.772	0.675	0.231	126	2.90	9.44	0.75	9.91
R15TS184	Alkali basalt	0.022	2.65	148	339	0.891	0.423	0.145	96.3	2.42	7.37	0.53	6.71
R14TS026a	Alkali basalt	0.239	5.93	123	496	2.88	1.11	0.577	153	3.56	10.9	0.78	14.6
R15DS105	Alkali basalt	0.061	3.52	56.0	434	0.773	0.638	0.263	137	3.23	8.48	0.62	10.2
R15MS031	Alkali basalt	0.041	4.37	87.9	385	0.945	0.724	0.244	145	3.40	12.5	0.84	12.4
R14AC018	Alkali basalt	0.136	11.5	147	466	2.06	1.79	0.642	248	5.27	24.1	1.63	20.5
R15DD051	Alkali basalt	0.048	8.31	122	470	1.16	1.46	0.497	239	4.96	22.0	1.51	21.7
R15DS174	Alkali basalt	0.024	4.48	84.3	370	1.29	0.84	0.214	193	4.19	12.7	0.82	14.1
R14DS053	Alkali basalt	0.035	5.25	131	478	1.30	1.15	0.328	190	4.27	19.0	1.28	18.3
R15DD145	Alkali basalt	0.051	5.27	92.3	490	1.28	1.09	0.401	181	4.24	17.0	1.18	16.0
R15MS021	Alkali basalt	0.043	4.71	91.9	420	1.16	0.97	0.259	170	3.81	14.8	1.02	15.0
R14AC009	Alkali basalt	0.064	6.29	95.7	642	1.35	1.04	0.370	203	4.58	18.3	1.32	15.7
R14TS033	Alkali basalt	0.112	8.74	134	624	1.83	1.66	0.490	239	5.30	24.3	1.70	23.3
R14AC066	Alkali basalt	0.057	6.78	138	491	1.59	1.20	0.398	228	4.80	17.9	1.20	18.9
R14AC084	Alkali basalt	0.061	5.84	127	435	1.20	1.06	0.372	178	3.96	16.2	1.12	19.1
R14TS014a	Alkali basalt	0.288	9.82	162	627	2.58	1.63	0.709	210	4.61	19.4	1.35	20.3
R15DS097	Alkali basalt	0.092	7.32	126	639	1.47	1.35	0.564	219	4.80	20.3	1.42	19.7
R16MS057	Alkali basalt	0.035	5.27	102	523	1.53	1.17	0.393	206	4.63	17.6	1.26	19.1
R15TS169	Alkali basalt	0.075	10.3	145	519	2.40	2.00	0.556	298	6.26	26.3	1.78	27.9
R15TS191	Alkali basalt	0.028	6.25	129	576	1.62	1.32	0.307	228	5.02	20.9	1.42	21.3
R14AC069	Alkali basalt	0.091	8.57	116	576	1.59	1.35	0.447	227	4.96	21.0	1.45	20.2
R14AC068	Alkali basalt	0.067	7.31	120	533	1.62	1.29	0.434	225	4.90	17.4	1.19	19.7
R15MS029	Alkali basalt	0.090	9.67	144	572	2.14	1.79	0.590	288	6.22	25.5	1.70	29.4
R14DS020	Alkali basalt	0.074	7.40	151	543	1.86	1.35	0.490	253	5.43	21.3	1.40	25.3
R14AC058a	Alkali basalt	0.194	9.41	182	634	2.45	1.70	0.629	269	5.77	24.2	1.86	24.1
R15TS197	Alkali basalt	0.052	5.95	159	611	1.54	1.23	0.432	213	4.72	19.2	1.30	19.7
R15TS202	Alkali basalt	0.069	9.04	154	469	1.99	1.80	0.493	264	5.71	23.4	1.66	25.4
R15DD047	Alkali basalt	0.032	3.92	137	674	1.70	1.41	0.307	235	5.16	21.3	1.44	22.6
R14TS079	Alkali basalt	0.074	8.80	173	544	2.05	1.58	0.557	314	6.46	23.8	1.61	25.9
R14TS018	Hawaiite	0.125	12.1	223	549	2.54	2.23	0.740	316	6.66	33.1	2.15	32.9
R14TRO133	Hawaiite	0.092	9.64	220	590	2.56	1.94	0.608	337	7.26	27.1	1.83	35.7
R15MS017	Hawaiite	0.096	11.1	242	546	3.03	2.45	0.756	403	8.47	33.3	2.19	36.5
R15MS022	Hawaiite	0.109	10.1	178	593	2.17	1.87	0.642	288	6.14	29.9	1.98	30.4
R14AC101	Hawaiite	0.098	12.0	204	587	2.36	2.16	0.690	315	6.48	32.4	2.22	36.4
R15TS162	Hawaiite	0.133	13.2	226	605	2.66	2.30	0.732	338	7.08	35.6	2.27	40.7
R14AC072	Hawaiite	0.121	11.7	178	630	2.57	2.12	0.740	334	6.95	31.6	2.13	32.7
R15DS156	Hawaiite	0.104	11.8	221	532	2.42	1.96	0.670	381	7.92	35.0	2.32	32.2
R15MS008	Hawaiite	0.143	14.9	226	546	2.78	2.23	0.800	361	7.80	39.0	2.54	40.7

Ce	Pr	Nd	Sm	Eu	Gd	Tb	Dy	Ho	Er	Tm	Yb	Lu	Y	Sc	Ni	Cr	V
20.1	2.85	13.1	3.58	1.32	4.21	0.710	4.51	0.883	2.40	0.33	1.91	0.300	22.3	31.4	179	415	248
32.4	4.42	19.3	4.81	1.70	5.09	0.858	5.10	0.992	2.58	0.35	2.13	0.340	24.4	25.3	132	171	239
16.8	2.34	10.7	3.09	1.21	3.67	0.636	3.90	0.780	1.96	0.28	1.69	0.256	18.8	32.7	130	256	262
42.5	5.66	24.0	5.71	1.98	5.79	0.963	5.82	1.12	2.92	0.40	2.53	0.379	27.9	22.0	277	460	179
23.9	3.24	14.2	3.71	1.46	4.23	0.713	4.31	0.834	2.11	0.30	1.73	0.269	20.4	27.1	178	328	242
17.0	2.48	11.9	3.36	1.28	3.91	0.674	4.20	0.812	2.19	0.30	1.80	0.269	20.3	33.6	110	227	267
34.2	4.61	20.1	4.99	1.79	5.28	0.844	4.88	0.944	2.40	0.33	1.92	0.277	23.6	27.4	164	267	277
25.6	3.60	16.2	4.14	1.59	4.59	0.760	4.56	0.869	2.27	0.30	1.76	0.264	21.0	29.7	163	295	300
30.7	4.33	19.5	5.00	1.87	5.47	0.910	5.41	1.04	2.70	0.36	2.20	0.331	25.6	28.4	186	237	237
45.7	5.91	24.5	5.89	1.98	5.88	0.962	5.73	1.14	2.93	0.40	2.52	0.372	27.8	25.3	155	309	205
49.1	6.30	25.8	5.86	2.03	5.87	0.942	5.73	1.08	2.84	0.39	2.37	0.350	27.2	21.1	207	257	180
34.4	4.75	20.9	5.23	1.89	5.63	0.929	5.69	1.10	2.86	0.39	2.40	0.378	27.1	29.1	112	155	251
43.3	5.94	25.8	6.41	2.30	6.52	1.04	6.23	1.21	3.02	0.41	2.45	0.377	29.2	25.2	149	227	217
38.2	5.28	23.3	5.69	2.07	5.98	0.995	5.90	1.16	2.99	0.42	2.49	0.371	27.7	28.5	103	150	277
35.8	4.85	21.5	5.34	2.04	5.72	0.939	5.64	1.10	2.81	0.38	2.29	0.342	26.9	27.7	117	217	246
36.8	4.94	21.8	5.27	2.01	5.24	0.858	4.84	0.93	2.34	0.31	1.90	0.285	22.0	24.8	128	145	314
53.0	7.00	29.0	6.65	2.42	6.47	1.01	5.83	1.10	2.84	0.37	2.23	0.340	27.0	24.6	96	120	284
44.8	6.09	26.7	6.54	2.39	6.49	1.03	6.07	1.19	2.99	0.39	2.36	0.385	28.5	25.1	75	130	224
46.6	6.48	29.7	7.06	2.69	7.32	1.14	6.71	1.27	3.21	0.43	2.53	0.390	31.7	27.7	106	151	230
46.0	6.10	25.8	6.12	2.10	5.98	0.947	5.46	1.03	2.57	0.35	2.08	0.312	25.5	22.7	84	66	298
45.9	6.06	25.9	6.20	2.24	6.14	0.959	5.60	1.03	2.68	0.36	2.13	0.315	25.9	24.5	74	74	315
45.0	6.11	26.4	6.41	2.35	6.58	1.06	6.13	1.18	2.93	0.40	2.43	0.370	29.0	24.7	76	89	266
62.9	8.01	33.1	7.37	2.55	7.12	1.14	6.69	1.29	3.27	0.46	2.80	0.433	31.8	21.7	83	154	188
49.5	6.58	28.3	6.78	2.42	6.53	1.04	6.10	1.17	2.93	0.40	2.46	0.368	28.6	23.7	76	65	260
47.6	6.36	27.4	6.53	2.38	6.36	1.03	5.97	1.17	2.92	0.39	2.40	0.358	27.9	25.0	55	78	276
46.3	6.06	26.2	6.10	2.32	6.22	0.990	5.87	1.14	2.90	0.39	2.40	0.363	27.5	22.4	56	31	235
68.7	9.21	39.0	8.83	3.06	8.67	1.35	7.65	1.47	3.72	0.49	2.95	0.453	35.8	19.9	91	101	168
61.7	8.49	37.4	8.71	3.15	8.74	1.36	7.64	1.46	3.60	0.48	2.85	0.432	36.0	24.7	53	66	219
58.4	7.84	34.5	7.68	2.83	7.49	1.15	6.54	1.24	3.12	0.41	2.49	0.368	30.2	22.2	32	7.8	234
46.3	6.32	27.1	6.56	2.39	6.57	1.03	6.08	1.16	2.95	0.39	2.43	0.367	28.2	23.1	49	5.0	329
59.5	7.91	33.7	7.80	2.71	7.74	1.21	7.23	1.37	3.55	0.48	2.83	0.433	34.3	23.7	51	95	192
53.5	7.15	31.4	7.32	2.67	7.38	1.14	6.59	1.27	3.21	0.43	2.58	0.379	31.0	21.4	40	4.0	244
60.9	8.16	34.6	8.04	2.80	7.89	1.25	7.35	1.39	3.59	0.49	2.97	0.433	35.1	22.0	37	12	201
76.1	10.0	42.7	9.46	3.30	9.22	1.43	8.02	1.50	3.78	0.50	3.02	0.463	37.1	22.3	64	97	158
85.4	11.9	51.8	11.7	4.11	11.2	1.70	9.73	1.83	4.49	0.60	3.54	0.520	44.0	21.7	37	39	148
83.5	10.9	45.0	9.99	3.37	9.49	1.49	8.73	1.69	4.29	0.61	3.68	0.570	41.7	20.1	37	30	153
70.9	9.59	41.0	9.55	3.34	9.30	1.40	8.26	1.55	3.87	0.52	3.14	0.473	38.3	22.3	17	1.0	204
86.5	11.8	50.9	11.5	3.96	11.2	1.68	9.48	1.77	4.36	0.58	3.36	0.506	43.8	19.9	26	17	143
96.5	13.1	56.8	12.8	4.42	12.1	1.84	10.6	1.97	4.76	0.62	3.67	0.547	47.7	18.6	18	6.1	124
76.2	10.0	42.6	9.69	3.40	9.15	1.41	8.04	1.51	3.73	0.50	3.02	0.431	36.8	18.8	7.4	0	156
76.6	10.1	42.8	9.95	3.36	9.54	1.53	9.05	1.74	4.43	0.62	3.82	0.598	42.8	20.7	14	0	158
97.8	13.2	57.4	13.0	4.33	12.4	1.93	11.2	2.09	5.33	0.72	4.18	0.655	51.9	16.7	9.3	0	85

Table 2. Trace-element concentrations, in parts per million by weight, of northern Harrat Rahat volcanic rocks analyzed for isotopic composition.—Continued

Sample	Type	Cs	Rb	Ba	Sr	Pb	Th	U	Zr	Hf	Nb	Ta	La
R14DS003	Mugearite	0.140	14.3	288	603	2.88	2.54	0.862	415	8.58	38.7	2.54	46.4
R14AC002	Mugearite	0.134	18.6	317	537	3.62	3.20	1.08	471	9.49	44.2	2.86	49.3
R14TS037	Mugearite	0.209	20.1	329	516	4.09	3.43	1.04	509	10.2	46.4	2.93	49.7
R14AC095	Mugearite	0.141	17.8	289	457	3.52	2.94	1.01	550	10.6	45.2	2.97	48.8
R14AC048	Mugearite	0.200	19.1	399	471	4.46	3.35	1.10	546	11.3	49.1	3.19	52.4
R14AC096	Mugearite	0.218	20.0	293	560	4.38	3.89	1.01	511	10.5	44.9	3.07	50.0
R14AC021	Mugearite	0.207	21.3	359	413	3.05	3.48	1.20	532	10.8	40.6	2.56	49.4
R16DD270	Mugearite (Hy)	0.169	24.7	440	579	5.16	3.71	1.36	769	14.9	53.7	3.23	57.8
R14AC019	Benmoreite	0.224	23.2	377	390	4.49	3.58	1.15	552	11.0	41.2	2.62	49.4
R14AC090	Benmoreite	0.220	23.8	394	341	5.04	3.91	1.22	599	12.2	43.9	2.79	51.6
R14AC027	Benmoreite	0.141	23.4	432	364	5.12	3.68	0.85	756	14.5	53.2	3.24	57.7
R14AC013	Benmoreite	0.318	28.0	1,029	211	4.69	4.10	1.02	669	12.9	42.3	2.82	46.5
R14AC003	Benmoreite	0.346	33.0	467	313	5.61	4.84	1.64	879	16.6	65.5	4.08	63.0
R14AC081	Benmoreite	0.319	31.3	430	359	7.22	5.05	1.72	826	16.4	71.2	4.80	61.7
R14AC082	Benmoreite	0.387	34.0	618	259	7.09	5.33	1.82	900	17.3	67.0	4.22	61.3
R15MS010	Trachyte	0.569	80.8	11.6	49.5	21.7	18.0	3.82	1,743	41.2	120	9.68	148
R14TS070	Trachyte	0.360	30.7	1,111	106	5.40	4.16	0.91	729	13.9	44.4	2.95	46.3
R14TRO050	Trachyte	0.326	43.0	478	100	8.84	6.45	2.18	1,275	24.4	97.3	5.56	74.5
R14AC046	Trachyte	0.296	32.7	871	163	9.28	5.34	0.84	1,064	20.3	73.5	4.32	65.7
R14AC010a	Trachyte	0.826	67.5	106	61.9	16.8	12.2	3.99	1,665	35.2	138	9.12	122
R14AC070	Trachyte	0.717	71.9	48.7	15.1	19.0	17.5	4.30	1,436	31.8	125	8.73	121
R14AC025	Trachyte	2.00	117	9.50	64.2	29.3	25.9	7.26	2,084	50.2	210	15.8	192
R14TS068	Trachyte	0.603	61.3	25.8	18.6	13.4	10.6	3.32	1,633	33.4	119	7.78	118
R14TRO038	Trachyte	0.438	50.2	56.6	10.9	9.43	6.91	2.38	1,058	22.1	74.2	4.92	73.9
R14TS028	Trachyte	1.01	85.0	14.3	7.4	21.0	15.8	5.05	2,120	44.8	175	11.1	147
R14AC051	Trachyte	0.572	67.4	31.0	15.6	15.6	11.9	3.81	1,797	36.4	134	8.63	111
R14AC035	Trachyte (Hy)	1.44	110	6.30	11.1	29.2	24.7	7.55	2,054	50.4	206	15.9	190
R14AC016	Trachyte (Hy, Qtz)	1.96	135	26.5	30.6	37.2	30.2	10.0	2,870	66.6	281	20.5	220

[a]Sample has anomalously high CaO/Al_2O_3 or Cs/Rb, indicative of residual secondary minerals in the split analyzed for chemical composition.

are corrected for fractionation to $^{179}Hf/^{177}Hf = 0.7325$. Repeated measurements of Nd standard La Jolla and Hf standard JMC-475 yielded an average value of $^{143}Nd/^{144}Nd = 0.511839\pm36$ ppm (n=110, 2σ) and $^{176}Hf/^{177}Hf = 0.282147\pm47$ ppm (n=108, 2σ). $^{143}Nd/^{144}Nd$ and $^{176}Hf/^{177}Hf$ ratios of the samples are reported relative to the accepted ratio of the standard—that is, $^{143}Nd/^{144}Nd = 0.511850$ for standard La Jolla and $^{176}Hf/^{177}Hf = 0.282160$ for standard JMC-475.

Results

The isotopic compositions of the Harrat Rahat samples are reported in table 3 and are available digitally from Salters and Sisson (2023). Volcanic rocks, especially the least evolved ones, show a limited range in isotopic composition. The Sr isotopic composition of most samples ranges from $^{87}Sr/^{86}Sr = 0.702871$ to 0.703231, whereas the evolved trachytes are as great as 0.706410. Nd isotopic compositions show a very limited range of $^{143}Nd/^{144}Nd = 0.512939$ to 0.513001, or a range of 1.2 ε_{Nd}, where ε is the deviation of the isotopic composition of the sample from that of the chondritic uniform reservoir (CHUR) in parts per 10,000. The range in Hf isotopic composition is limited to 2 ε_{Hf} units with $^{176}Hf/^{177}Hf$ ranging from 0.283045 to 0.283102. Even within this limited range, Hf and Nd isotopic compositions are well correlated. The Pb isotopic composition shows

Ce	Pr	Nd	Sm	Eu	Gd	Tb	Dy	Ho	Er	Tm	Yb	Lu	Y	Sc	Ni	Cr	V
111	15.1	64.5	14.4	4.84	13.3	2.01	11.4	2.09	5.23	0.70	4.14	0.638	52.0	17.1	7.7	0	90
115	15.2	64.6	14.3	4.64	13.0	1.99	11.3	2.07	5.22	0.70	4.19	0.637	51.3	14.9	2.6	0	75
115	15.2	63.6	13.7	4.55	12.9	1.92	11.1	2.06	5.29	0.71	4.19	0.654	51.8	15.0	3.9	0	67
111	14.2	57.4	12.2	3.83	11.6	1.85	10.9	2.05	5.40	0.74	4.62	0.744	51.2	13.9	3.8	0	53
119	15.6	64.5	14.1	4.62	13.2	2.11	12.2	2.38	6.09	0.86	5.26	0.843	58.8	16.8	2.5	0	23
113	14.7	59.3	13.0	4.28	11.7	1.84	10.5	2.00	5.14	0.70	4.31	0.677	49.9	10.5	2.1	0.9	22
112	14.6	59.4	12.9	4.16	11.6	1.81	10.6	2.02	5.24	0.73	4.58	0.688	50.1	12.0	2.8	0.2	36
131	17.0	68.7	15.0	4.60	13.6	2.17	13.0	2.48	6.56	0.92	5.73	0.914	61.8	14.6	2.9	0.0	8.6
113	14.5	58.8	12.8	4.14	11.4	1.80	10.5	1.99	5.24	0.72	4.58	0.710	49.7	11.0	2.9	1.0	30
117	15.0	59.3	12.8	3.99	11.2	1.81	10.5	2.04	5.29	0.75	4.77	0.756	50.2	10.3	0.1	0	15
131	16.9	68.6	14.9	4.56	13.6	2.22	12.8	2.49	6.52	0.92	5.70	0.896	61.3	14.2	1.7	0.6	6.2
104	13.2	52.1	11.3	4.61	10.5	1.71	10.4	2.08	5.64	0.83	5.25	0.907	52.3	17.5	5.1	2.5	7.2
135	16.1	60.8	12.5	3.55	10.7	1.80	11.0	2.21	5.97	0.90	5.92	0.944	55.9	7.9	0.7	2.4	3.4
134	16.2	61.8	12.5	3.71	10.9	1.83	11.3	2.25	6.19	0.94	6.23	0.992	57.9	5.4	1.6	1.4	3.0
133	16.3	62.9	12.8	4.05	11.5	1.96	11.7	2.33	6.32	0.93	5.92	0.945	57.6	11.0	1.1	1.5	4.3
300	30.3	99.2	18.9	1.75	17.3	3.39	22.0	4.52	13.0	2.06	13.4	2.08	120	0.2	2.6	3.7	5.5
102	12.7	50.6	10.7	4.36	9.88	1.66	10.2	1.99	5.58	0.83	5.42	0.884	50.3	16.1	3.3	0.9	5.0
164	20.1	75.6	15.4	3.01	13.7	2.35	14.4	2.89	7.86	1.18	7.62	1.22	72.7	4.3	0.3	1.4	3.9
146	18.3	70.0	15.1	4.47	13.4	2.32	14.4	2.84	7.82	1.17	7.60	1.28	69.9	13.6	1.4	2.6	6.6
248	28.5	101	20.6	2.47	17.9	3.35	20.9	4.26	12.0	1.79	11.8	1.77	110.4	1.4	3.5	4.8	5.0
249	27.9	97.1	19.0	2.05	16.8	3.15	20.9	4.38	12.8	1.90	12.5	1.96	114.2	1.1	1.8	2.5	3.5
384	41.4	140	27.7	2.00	25.0	4.83	32.3	6.79	19.9	3.03	19.7	2.87	180.9	0.3	1.7	3.2	1.9
241	27.8	98.2	19.1	2.25	17.1	3.05	19.2	3.94	11.3	1.70	11.1	1.75	102.3	0.6	2.6	3.8	1.4
159	19.8	74.8	15.6	2.44	13.7	2.39	14.3	2.86	7.90	1.19	7.80	1.25	71.9	2.7	3.2	0.5	1.0
304	35.9	128	25.7	3.03	23.7	4.23	26.5	5.43	15.1	2.28	14.6	2.18	141.3	0.1	2.7	3.0	3.1
237	28.1	102	21.0	2.60	18.5	3.33	20.9	4.24	11.9	1.81	11.7	1.89	110	1.6	1.9	1.4	2.0
376	41.4	139	27.7	2.01	25.2	4.83	31.4	6.54	18.9	2.88	18.5	2.87	173.5	0.4	1.7	2.1	1.8
462	54.2	194	41.1	4.78	37.8	6.90	44.2	9.21	25.8	3.75	23.7	3.54	237.2	0.7	3.9	3.2	2.7

small but correlated variations, with $^{206}Pb/^{204}Pb$ ranging from 18.5088 to 18.8085, $^{207}Pb/^{204}Pb$ ranging from 15.4972 to 15.5353, and $^{208}Pb/^{204}Pb$ ranging from 18.1258 to 18.4889.

Within the limited range of Nd isotopic composition, the least radiogenic Sr values are negatively correlated with $^{143}Nd/^{144}Nd$, and the range of Harrat Rahat samples broadens toward more radiogenic Sr among the less evolved magmas at the unradiogenic Nd end (fig. 2). The highly evolved magmas have $^{87}Sr/^{86}Sr$ values that are much more radiogenic, although their Nd isotopic compositions do not vary. Hf and Nd isotopic compositions are well correlated (fig. 3), and the slope of ε_{Hf} versus ε_{Nd} is 1.32 (not shown), similar to the slope for the variation in MORB and other terrestrial volcanic rocks (Vervoort and others, 1999).

The Pb isotope values (fig. 4) straddle the Northern Hemisphere Reference Line (NHRL) of Hart (1984). The least evolved magmas have the most radiogenic Pb isotopic compositions. There is a positive correlation between Mg number (Mg# = Mg/[Mg+Fe^{2+}], molar) and $^{206}Pb/^{204}Pb$ and $^{208}Pb/^{204}Pb$ (fig. 5). Although both Pb and Sr isotopic compositions show a change in values in the evolved magmas, the two isotope systems are not correlated. This indicates that the Sr/Pb ratio of the magmas decreased during fractionation, which is expected with the crystallization of feldspars.

Table 3. Isotopic compositions of volcanic rocks from northern Harrat Rahat.

[Rock types are classified as in Cox and others (1979); Hy and Qtz indicate CIPW normative hypersthene and quartz; all other samples are nepheline normative. Isotopic values can be obtained digitally from Salters and Sisson (2023). Trans., transitional]

Sample	Type	$^{87}Sr/^{86}Sr$	$^{143}Nd/^{144}Nd$	$^{176}Hf/^{177}Hf$	$^{206}Pb/^{204}Pb$	$^{207}Pb/^{204}Pb$	$^{208}Pb/^{204}Pb$	$^{208}Pb/^{206}Pb$	$^{207}Pb/^{206}Pb$
R14AC052	Trans. basalt (Hy)	0.703215	0.512966	0.283064	18.7286	15.5232	38.2161	2.040666	0.828835
R14AC088	Trans. basalt (Hy)	0.702969	0.512971	0.283062	18.6055	15.5170	38.2135	2.053931	0.833985
R15DS124	Alkali basalt	0.702996	0.512983	0.283083	18.8085	15.5294	38.4889	2.046583	0.825711
R14AC022	Alkali basalt	0.702962	0.512978	0.283086	18.7931	15.5224	38.4713	2.047176	0.825932
R14TS001	Alkali basalt	0.702913	0.512964	0.283094	18.6921	15.5058	38.3778	2.053151	0.829501
R15TS184	Alkali basalt	0.702948	0.512954	0.283071	18.6742	15.5305	38.3158	2.051815	0.831629
R14TS026	Alkali basalt	0.702939	0.512971	0.283067	18.7159	15.5353	38.4331	2.053726	0.830112
R15DS105	Alkali basalt	0.702915	0.512988	0.283081	18.6557	15.5148	38.3224	2.054232	0.831618
R15MS031	Alkali basalt	0.702928	0.512980	0.283087	18.7057	15.5141	38.3873	2.052189	0.829354
R14AC018	Alkali basalt	0.703074	0.512939	0.283098	18.7645	15.5288	38.4016	2.046512	0.827541
R15DD051	Alkali basalt	0.702995	0.512977	0.283076	18.7880	15.5160	38.4711	2.047685	0.825819
R15DS174	Alkali basalt	0.702891	0.512987	0.283088	18.6365	15.5067	38.2937	2.053067	0.830841
R14DS053	Alkali basalt	0.703210	0.512984	0.283080	18.7411	15.5205	38.4246	2.050280	0.828153
R15DD145	Alkali basalt	0.703231	0.512984	0.283087	18.7183	15.5115	38.3708	2.049950	0.828655
R15MS021	Alkali basalt	0.702938	0.512983	0.283100	18.7502	15.5212	38.4451	2.054171	0.829891
R14AC009	Alkali basalt	0.702999	0.512990	0.283088	18.6743	15.5056	38.3601	2.054206	0.830295
R14TS033	Alkali basalt	0.702929	0.512968	0.283073	18.7261	15.5174	38.4043	2.050798	0.828605
R14AC066	Alkali basalt	0.702909	0.512982	0.283074	18.6382	15.5063	38.2880	2.054292	0.831934
R14AC084	Alkali basalt	0.702984	0.512989	0.283070	18.6962	15.5079	38.3650	2.052021	0.829429
R14TS014	Alkali basalt	0.702931	0.512971	0.283062	18.7227	15.5342	38.4404	2.053370	0.829752
R15DS097	Alkali basalt	0.702901	0.512993	0.283092	18.6943	15.5147	38.4006	2.054171	0.829891
R16MS057	Alkali basalt	0.703010	0.512987	0.283080	18.7105	15.5095	38.3711	2.050800	0.828892
R15TS169	Alkali basalt	0.703099	0.512983	0.283079	18.7060	15.5120	38.3630	2.050851	0.829222
R15TS191	Alkali basalt	0.702901	0.512986	0.283083	18.7165	15.5124	38.3911	2.051212	0.828785
R14AC069	Alkali basalt	0.702871	0.513001	0.283088	18.6728	15.4978	38.3321	2.052828	0.829948
R14AC068	Alkali basalt	0.702915	0.512992	0.283092	18.6556	15.4972	38.3075	2.053470	0.830696
R15MS029	Alkali basalt	0.702925	0.512986	0.283099	18.6923	15.5071	38.3715	2.052815	0.829572
R14DS020	Alkali basalt	0.702899	0.512977	0.283077	18.6309	15.5079	38.2983	2.055666	0.832353
R14AC058	Alkali basalt	0.702999	0.512969	0.283074	18.6485	15.5153	38.3230	2.055052	0.831980
R15TS197	Alkali basalt	0.702889	0.512992	0.283102	18.6695	15.5083	38.3467	2.053991	0.830650
R15TS202	Alkali basalt	0.702969	0.512980	0.283081	18.6612	15.5119	38.3330	2.054166	0.831211
R15DD047	Alkali basalt	0.702912	0.512990	0.283078	18.6728	15.5145	38.3357	2.053067	0.830841
R14TS079	Alkali basalt	0.702923	0.512980	0.283067	18.6321	15.5046	38.2871	2.054917	0.832115
R14TS018	Hawaiite	0.702936	0.512983	0.283073	18.7021	15.5188	38.3826	2.052358	0.829766
R14TRO133	Hawaiite	0.702886	0.512974	0.283072	18.5875	15.5062	38.2453	2.057616	0.834205
R15MS017	Hawaiite	0.702939	0.512994	0.283087	18.6691	15.5122	38.3512	2.049950	0.828655
R15MS022	Hawaiite	0.702943	0.512990	0.283099	18.6974	15.5125	38.3809	2.052760	0.829637
R14AC101	Hawaiite	0.702900	0.512988	0.283072	18.6853	15.5074	38.3545	2.052699	0.829906
R15TS162	Hawaiite	0.702880	0.512977	0.283084	18.6838	15.5088	38.3617	2.053224	0.830041
R14AC072	Hawaiite	0.702888	0.513001	0.283083	18.6869	15.5031	38.3587	2.052698	0.829601
R15DS156	Hawaiite	0.702960	0.512929	0.283069	18.6506	15.5127	38.3194	2.054603	0.831735
R15MS008	Hawaiite	0.702944	0.512951	0.283076	18.6963	15.5131	38.3828	2.052938	0.829709
R14DS003	Mugearite	0.702899	0.512977	0.283072	18.6372	15.5141	38.3185	2.056067	0.832403
R14AC002	Mugearite	0.702996	0.512970	0.283074	18.6360	15.5083	38.3021	2.055299	0.832139

Table 3. Isotopic compositions of volcanic rocks from northern Harrat Rahat.—Continued

Sample	Type	$^{87}Sr/^{86}Sr$	$^{143}Nd/^{144}Nd$	$^{176}Hf/^{177}Hf$	$^{206}Pb/^{204}Pb$	$^{207}Pb/^{204}Pb$	$^{208}Pb/^{204}Pb$	$^{208}Pb/^{206}Pb$	$^{207}Pb/^{206}Pb$
R14TS037	Mugearite	0.705204	0.512976	0.283072	18.6202	15.5068	38.2791	2.055818	0.832772
R14AC095	Mugearite	0.702934	0.512960	0.283074	18.6831	15.5079	38.3524	2.052804	0.830020
R14AC048	Mugearite	0.702918	0.512964	0.283057	18.5781	15.5075	38.2102	2.056773	0.834692
R14AC096	Mugearite	0.702924	0.512966	0.283076	18.6642	15.5139	38.3450	2.054475	0.831193
R14AC021	Mugearite	0.702918	0.512977	0.283072	18.6257	15.5170	38.3210	2.057452	0.833073
R16DD270	Mugearite (Hy)	0.702917	0.512973	0.283063	18.5903	15.5089	38.2518	2.057633	0.834224
R14AC019	Benmoreite	0.702926	0.512968	0.283071	18.6205	15.5086	38.2911	2.056450	0.832869
R14AC090	Benmoreite	0.702918	0.512988	0.283078	18.6168	15.5096	38.2945	2.057007	0.833078
R14AC027	Benmoreite	0.702962	0.512962	0.283065	18.5932	15.5096	38.2568	2.057593	0.834124
R14AC013	Benmoreite	0.702978	0.512963	0.283076	18.5247	15.5089	38.1649	2.060225	0.837185
R14AC003	Benmoreite	0.702920	0.512968	0.283079	18.6191	15.5130	38.2761	2.055752	0.833152
R14AC081	Benmoreite	0.702969	0.512979	0.283078	18.5806	15.5040	38.1781	2.054744	0.834389
R14AC082	Benmoreite	0.702883	0.512980	0.283062	18.6023	15.5072	38.2275	2.055010	0.833595
R15MS010	Trachyte	0.704640	0.512969	0.283067	18.5821	15.5106	38.2504	2.058456	0.834707
R14TS070	Trachyte	0.703057	0.512965	0.283057	18.5088	15.5014	38.1258	2.059896	0.837489
R14TRO050	Trachyte	0.703374	0.512972	0.283060	18.5732	15.5109	38.2349	2.058636	0.835100
R14AC046	Trachyte	0.702997	0.512953	0.283056	18.5446	15.5078	38.1671	2.058149	0.836225
R14AC010	Trachyte	0.704389	0.512949	0.283061	18.5499	15.5159	38.2276	2.060811	0.836415
R14AC070	Trachyte	0.703301	0.512967	0.283062	18.5334	15.5056	38.1882	2.060561	0.836615
R14AC025	Trachyte	0.705344	0.512961	0.283045	18.5248	15.5097	38.1923	2.061712	0.837215
R14TS068	Trachyte	0.704518	0.512959	0.283051	18.5663	15.5104	38.2343	2.059341	0.835377
R14TRO038	Trachyte	0.704022	0.512956	0.283051	18.5433	15.5086	38.1955	2.059827	0.836321
R14TS028	Trachyte	0.703383	0.512956	0.283048	18.5011	15.5091	38.1483	2.061976	0.838257
R14AC051	Trachyte	0.704684	0.512956	0.283055	18.5069	15.5073	38.1517	2.061513	0.837899
R14AC035	Trachyte (Hy)	0.704624	0.512947	0.283054	18.5289	15.5141	38.2073	2.062031	0.837265
R14AC016	Trachyte (Hy, Qtz)	0.706410	0.512946	0.283046	18.5220	15.5149	38.1921	2.061995	0.837628

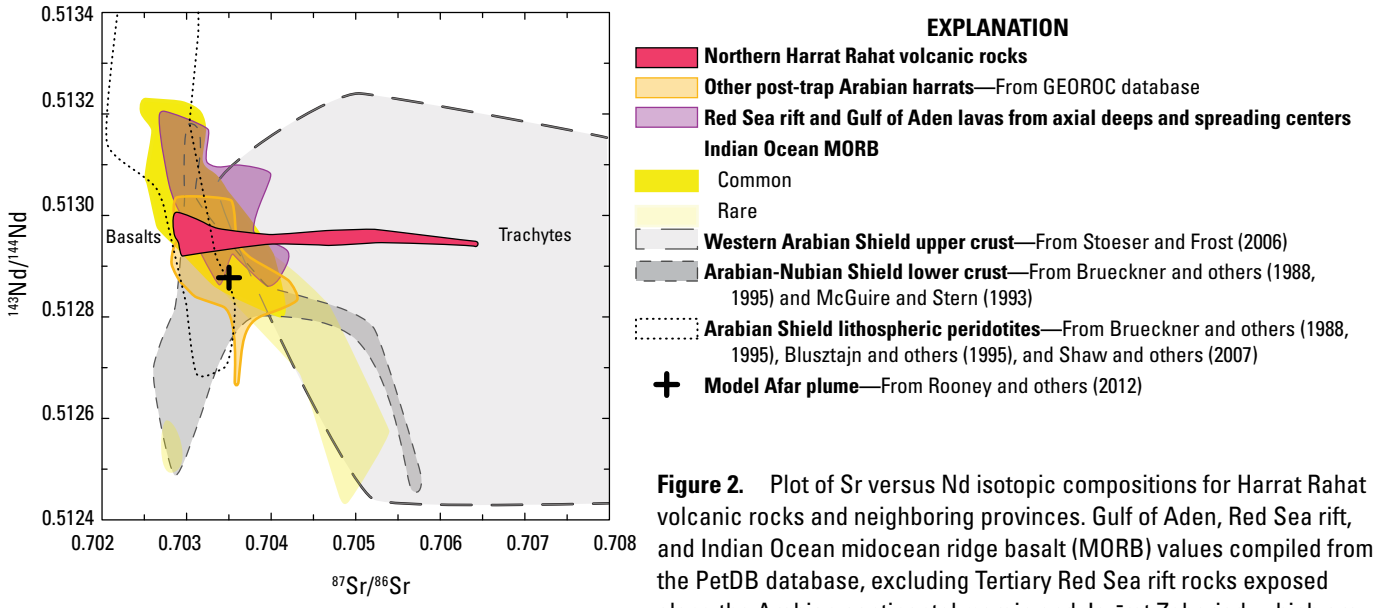

Figure 2. Plot of Sr versus Nd isotopic compositions for Harrat Rahat volcanic rocks and neighboring provinces. Gulf of Aden, Red Sea rift, and Indian Ocean midocean ridge basalt (MORB) values compiled from the PetDB database, excluding Tertiary Red Sea rift rocks exposed along the Arabian continental margin and Jazīrat Zabarjad, which are influenced by crustal assimilation and alteration.

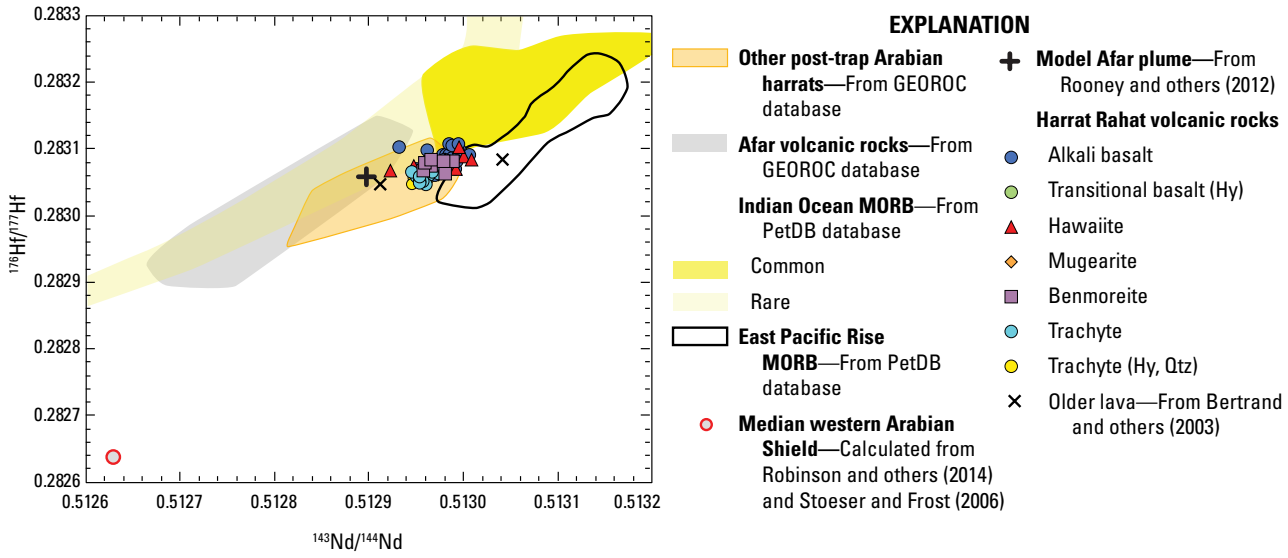

Figure 3. Plot of Nd versus Hf isotopic compositions for Harrat Rahat volcanic rocks and neighboring provinces. Harrat Rahat samples are divided by rock type (see table 1), where Hy and Qtz designate normative hypersthene and quartz; all other samples are nepheline normative. MORB, midocean ridge basalt.

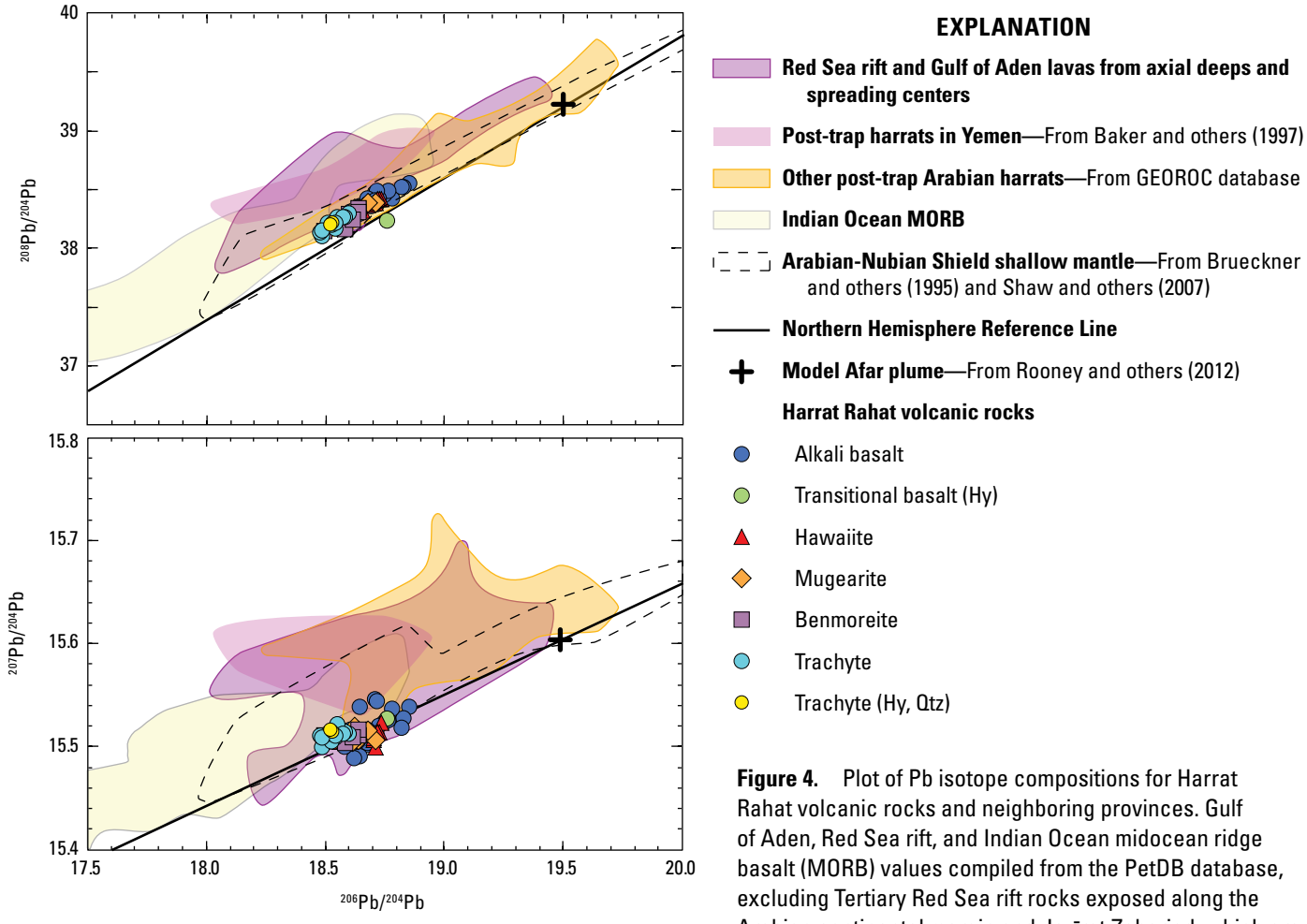

Figure 4. Plot of Pb isotope compositions for Harrat Rahat volcanic rocks and neighboring provinces. Gulf of Aden, Red Sea rift, and Indian Ocean midocean ridge basalt (MORB) values compiled from the PetDB database, excluding Tertiary Red Sea rift rocks exposed along the Arabian continental margin and Jazīrat Zabarjad, which are influenced by crustal assimilation and alteration.

Discussion

Here we use isotopic compositions and major- and trace-element concentrations to assess the source conditions of the Harrat Rahat magmas. A first step is to determine to what extent the variations are affected by crustal-level processes. The narrow range in Nd, Hf, and Pb isotopic compositions indicates that the mantle source for the Harrat Rahat magmas is rather homogeneous.

Crustal Contamination

The high $^{87}Sr/^{86}Sr$ in the evolved trachytes indicates that crustal contamination took place, certainly at the most advanced differentiation stages. On an Mg# versus $^{87}Sr/^{86}Sr$ diagram (fig. 5), significant contamination by crustal material is only apparent at Mg# <0.1. These are trachytes with low Sr concentrations (7–64 ppm), owing to alkali feldspar fractionation, and so were more readily modified in Sr isotopes than were the less evolved magmas. Crustal interaction also took place at earlier differentiation stages and in a progressive fashion, as is shown by the high-precision Pb isotope measurements that vary consistently with Mg# (fig. 5). The composition of the material contaminating the magmas lowered the $^{206}Pb/^{204}Pb$ and $^{208}Pb/^{204}Pb$ values, but increased the $^{208}Pb/^{206}Pb$ values, and lies near the NHRL.

Major-element variations indicate that the magmas underwent fractionation chiefly at mid-crustal pressures by separation dominantly of olivine gabbroic cumulates, followed by titanomagnetite-plus-olivine gabbroic cumulates, and finally by late-stage separation of a syenitic assemblage yielding the volumetrically minor evolved trachytes (Sisson and others, 2023). The MgO versus Sr variation of Harrat Rahat magmas shows an inflection point around 6 weight percent MgO where Sr concentrations stop their modest increase with decreasing MgO, and a second inflection point at about 4 weight percent MgO where Sr concentrations decrease sharply with decreasing MgO. This indicates a

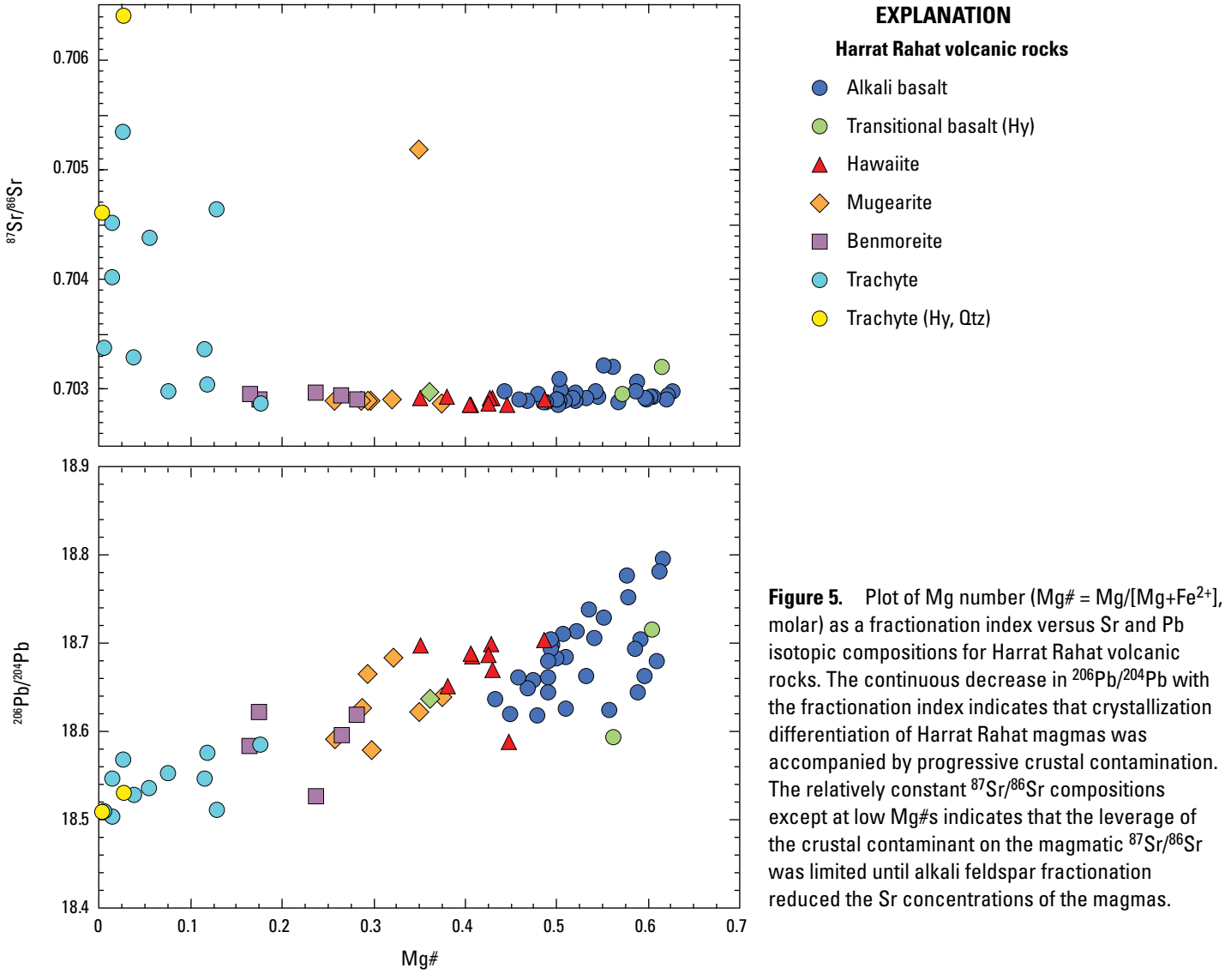

Figure 5. Plot of Mg number (Mg# = Mg/[Mg+Fe^{2+}], molar) as a fractionation index versus Sr and Pb isotopic compositions for Harrat Rahat volcanic rocks. The continuous decrease in $^{206}Pb/^{204}Pb$ with the fractionation index indicates that crystallization differentiation of Harrat Rahat magmas was accompanied by progressive crustal contamination. The relatively constant $^{87}Sr/^{86}Sr$ compositions except at low Mg#s indicates that the leverage of the crustal contaminant on the magmatic $^{87}Sr/^{86}Sr$ was limited until alkali feldspar fractionation reduced the Sr concentrations of the magmas.

change in the bulk mineral/melt partition coefficient for Sr (D_{Sr}), with the first inflection related to an increase in the crystallizing proportion of plagioclase and an increase in its albite component, and the second inflection owing to alkali feldspar appearing and subsequently dominating the crystallizing assemblage (Sisson and others, 2023). Since Pb and Sr isotopic compositions are not correlated, this indicates that the Pb isotopic composition of the contaminant was much different than the Pb isotopic composition of the mafic magma. The leverage that the contaminant had on the Pb isotopic composition was much larger than the leverage on Sr and Nd isotopic compositions, otherwise crustal contamination would be apparent in the Sr and Nd systems at earlier differentiation stages (higher Mg#) in the suite. This indicates that an unradiogenic lower-crustal-type Pb composition typifies the crustal contaminant. The Sr/Pb concentration ratio of the most primitive alkali basalts is about 400, whereas the Sr/Pb ratio of the evolved trachytes is about 0.7. This large change in Sr/Pb indicates that as crystal fractionation progressed, the leverage the crustal contaminant had on the Pb isotopic composition decreased as the magma's Pb concentration increased, whereas the leverage on the Sr isotopic composition increased as the magma's Sr concentration decreased. These changes dictate that assimilation fractional crystallization models should be used to understand the isotope evolution paths instead of simple mixing calculations.

Stoeser and Frost (2006) compiled radiogenic isotope data for Arabian Shield upper crustal terranes and Pb isotopic compositions of feldspars from, and galena associated with, exposed plutonic rocks. The Precambrian upper crust in the Harrat Rahat area consists mainly of juvenile arc plutonic and (meta)volcanic rocks, and (meta)sedimentary rocks derived therefrom, that formed and accreted to the continent between 740 and 700 Ma (Stoeser and Frost, 2006). Their initial Pb isotopic compositions, as recorded by low U/Pb material (feldspar and galena), were about $^{206}Pb/^{204}Pb = 17.5$, $^{207}Pb/^{204}Pb = 15.4$, and $^{208}Pb/^{204}Pb = 37.0$, which is near the NHRL. An estimate of the present-day bulk Precambrian crustal composition near Harrat Rahat can be obtained with the galena Pb values as an estimate of the initial Pb in the crust at 700 Ma, using upper or bulk continental crust U/Pb (Rudnick and Gao, 2014) to calculate subsequent radiogenic ingrowth. This results in a present-day $^{206}Pb/^{204}Pb$ of 18.9 and 18.6, respectively. Both estimates are clearly too high for Arabian upper or bulk crust to be the contaminant for the Harrat Rahat magmas. The lower crust of the Arabian-Nubian Shield is exposed on Jazīrat Zabarjad (Saint Johns Island; widely referred to as Zabargad Island in the earth science literature), western central Red Sea (fig. 1), and those gneisses have unradiogenic Pb (mean $^{206}Pb/^{204}Pb = 17.84$), but also unradiogenic Sr and Nd isotopic compositions averaging 0.7035 and 0.51265, respectively (Brueckner and others, 1988, 1995). McGuire and Stern (1993) also report Sr and Nd isotopic compositions of mafic granulites from the Arabian Shield's lower crust, carried up as xenoliths in harrat magmas (not from Harrat Rahat), that have average $^{87}Sr/^{86}Sr$ and $^{143}Nd/^{144}Nd$ values of 0.7033 and 0.51280. These Sr isotopic compositions from Jazīrat Zabarjad gneisses and the xenoliths are too low for such lower crustal rocks to be the crustal contaminant of the most evolved magmas of Harrat Rahat.

There are several simplified scenarios that can explain the observed isotopic variation. One possibility would involve two different contaminants: (1) a lower crustal component similar to rocks exposed on Jazīrat Zabarjad that results in the $^{206}Pb/^{204}Pb$ variation from 18.88 to 18.50, but has little influence on Sr and Nd isotopic compositions owing to their similarity to harrat magmas, followed by (2) late-stage selective contamination of the more evolved magmas with Arabian Shield upper crust, similar to compositions reported by Stoeser and Frost (2006). The selective aspect would be that the radiogenic Pb that is mostly harbored in zircons was not assimilated in the magma, so that the Pb isotopic composition of the upper crustal assimilate was unradiogenic ($^{206}Pb/^{204}Pb$ <18.4), similar to values measured in feldspars and galena of the exposed Arabian Shield. Speculatively, this might take place if the materials assimilated were crustal partial melts that left most zircons and their radiogenic Pb in the residual crystalline sources. The required amount of assimilation is small: a mass assimilated over mass crystallized ratio of 0.05 is used in the calculations. The bulk partition coefficient for Sr (D_{Sr}) changes from 0.4 to 1.5 after ~50 weight percent crystallization at approximately 6 weight percent MgO where plagioclase increases in its crystallizing proportion and becomes more sodic (Sisson and others, 2023), and then D_{Sr} changes from 1.5 to 4 at 4 weight percent MgO after ~75 weight percent crystallization when alkali feldspar joins and dominates the crystallizing assemblage. This model clearly has the elegance of matching the evolution with compositions that are observed locally. However, the results are far from unique, and with selective assimilation, however, one would expect to find other evidence of incomplete melting in the form of crustal xenocrysts, which have not been recognized.

From the isotopic variation it is clear that the crustal contaminants, on average, had $^{206}Pb/^{204}Pb$ of less than 18.4 and $^{87}Sr/^{86}Sr$ of 0.706 or higher. This combination of isotopic compositions is not typical for either the Arabian lower crust (too high $^{87}Sr/^{86}Sr$) or the bulk Arabian upper crust (too low $^{206}Pb/^{204}Pb$). The lower crust is, however, extremely variable in Sr, Nd, and Pb isotopic space and is relatively sparsely characterized (figs. 2 and 6). A second way of achieving the observed variation is with the same partition coefficients for Sr, Nd, and Pb, the same ratio of mass assimilated over mass crystallized, but with a single isotopic composition for the assimilate adjusted to yield a close match to the Harrat Rahat suite. This composition is within the range observed for the Arabian Shield, but is not typical for either its upper or lower crust. Table 4 lists the important parameters of the model and the composition of the "bulk" crustal assimilate. The trajectories the magmas would follow during assimilation fractional crystallization are shown in figure 7, employing the formulation by DePaolo (1981). Concentrations of the crustal contaminant were taken from lower crustal values of Rudnick and Gao

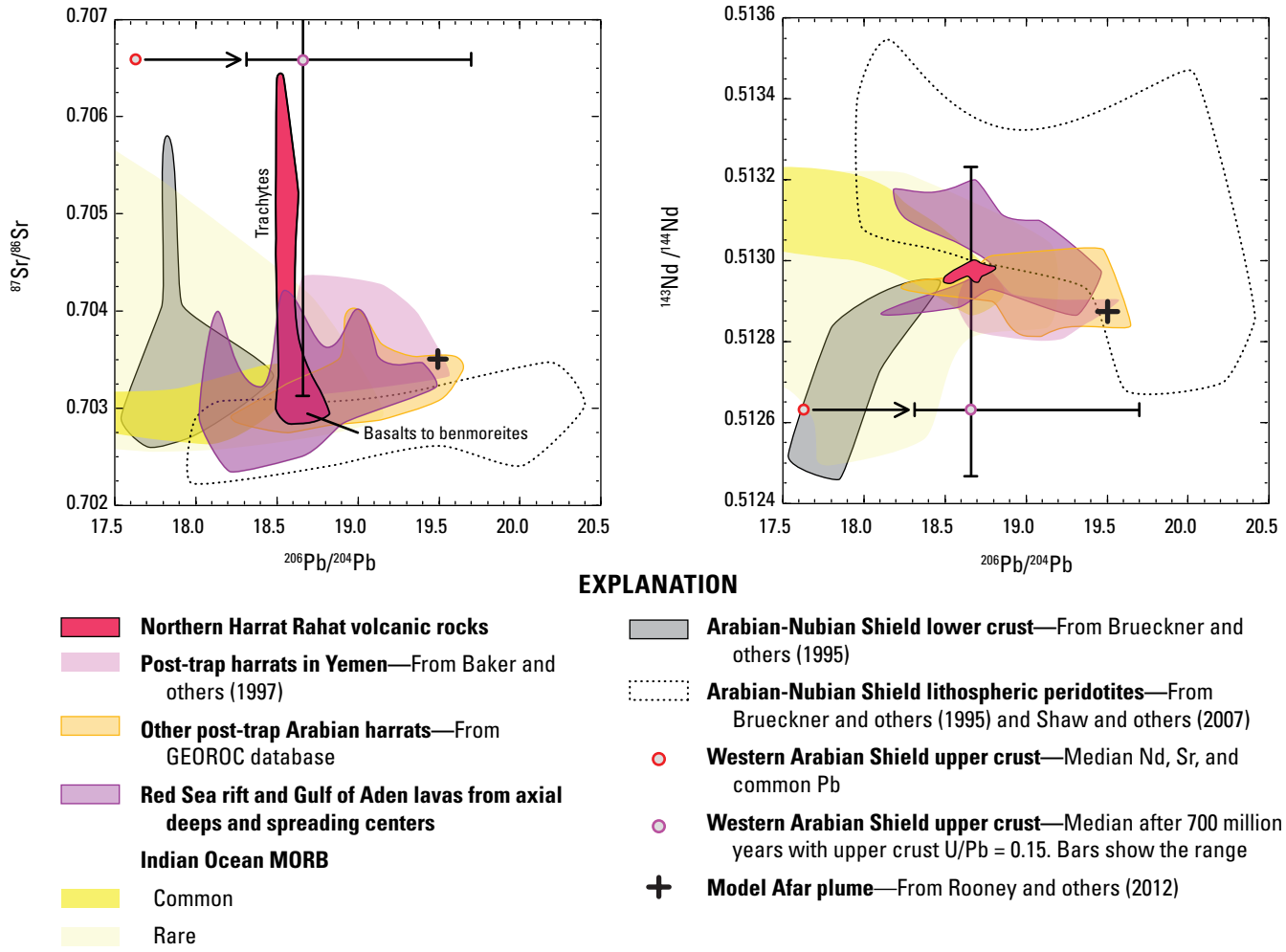

Figure 6. Plots of Pb-Sr and Pb-Nd isotopic compositions for Harrat Rahat volcanic rocks and neighboring provinces as well as for Arabian Shield crust and lithospheric upper mantle. Gulf of Aden, Red Sea rift, and Indian Ocean midocean ridge basalt (MORB) values compiled from the PetDB database, excluding Tertiary Red Sea rift rocks exposed along the Arabian continental margin and Jazīrat Zabarjad, which are influenced by crustal assimilation and alteration. Median of measured Sr, Nd, and common Pb for western Arabian Shield upper crust from Stoeser and Frost (2006) and recalculated for 700 million years of ^{206}Pb ingrowth for a whole-rock U/Pb of 0.15, typical for upper continental crust (Rudnick and Gao, 2014; Hacker and others, 2015). Note that some basalts of the active Red Sea rift and Gulf of Aden deviate to high $^{87}Sr/^{86}Sr$ and to low $^{143}Nd/^{144}Nd$ and $^{206}Pb/^{204}Pb$, possibly owing to assimilation of young sediments shed from the adjacent shields or assimilation of hydrothermal products carrying sediment isotopic compositions.

Table 4. Assimilation fractional crystallization parameters.

[ppmw, parts per million by weight; *D*, bulk partition coefficient; –, not applicable]

Component	$^{206}Pb/^{204}Pb$	Pb, ppmw	D_{Pb}	$^{143}Nd/^{144}Nd$	Nd, ppmw	D_{Nd}	$^{87}Sr/^{86}Sr$	Sr, ppmw	D_{Sr}
Basaltic parent A	18.82	0.9	0.28	0.512970	18	0.32	0.7029	320	0.4
Basaltic parent B	18.70	0.9	0.28	0.513002	18	0.32	0.7029	320	0.4
Stage 2 parent A	18.646	1.87	0.28	0.512962	26	0.32	0.70297	511	1.5
Stage 2 parent B	18.616	1.82	0.28	0.512993	26.1	0.32	0.70297	511	1.5
Stage 3 parent A	18.54	4.7	0.4	0.512954	26.1	0.32	0.70312	406	4
Stage 3 parent B	18.57	4.7	0.4	0.512894	26.1	0.32	0.70312	406	4
Assimilate	18.20	15.2	–	0.512630	18	–	0.707	282	–

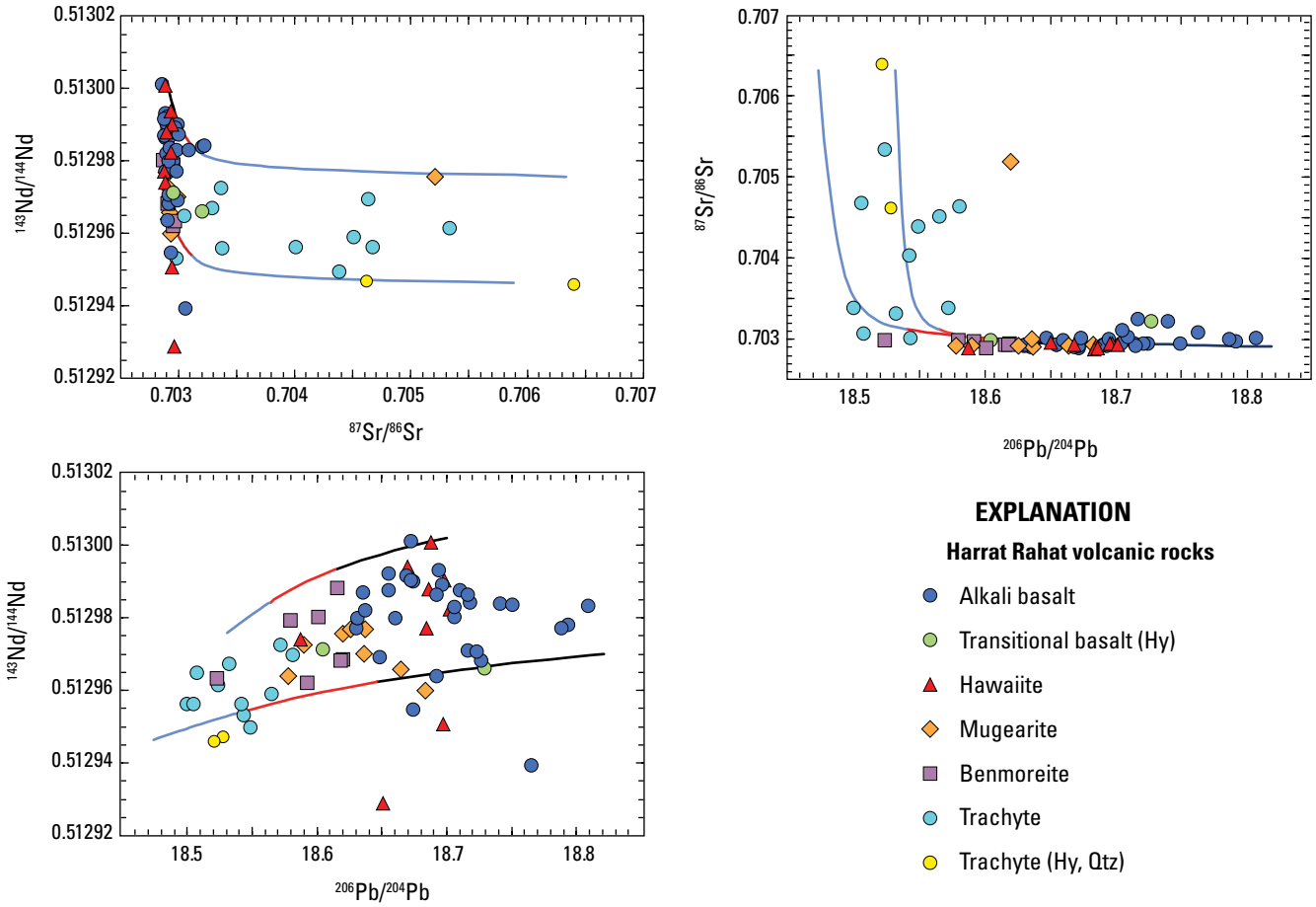

Figure 7. Plot showing an assimilation fractional crystallization model for Rahat Harrat magmas. Two evolution lines are indicated for two slightly different initial magma compositions. Details of the model parameters are in table 4. The model lines change color with the change in Sr partition coefficient from 0.4 (black), to 1.5 (red), to 4 (blue). The model with more radiogenic Nd isotopic composition for the least evolved magma is contaminated with a crustal component that has slightly more radiogenic Pb. The range in Nd composition for the most primitive magma is needed to explain the 0.6 ε_{Nd} range at almost constant $^{87}Sr/^{86}Sr$ and $^{206}Pb/^{204}Pb$, where ε is the deviation of the isotopic composition of the sample from that of the chondritic uniform reservoir (CHUR) in parts per 10,000.

(2014). Some diversity in the parental magmas, represented as basaltic parents A and B in table 4, is required to encompass the complete range of observed isotope values. Crystallizing assemblages are initially gabbroic, then evolved gabbroic (stage 2 in table 4), then syenitic (stage 3 in table 4), with melt compositions at the cumulate transitions given as parents A and B in stage 2 and 3 derived by assimilation-fractional crystallization from basaltic parents A and B, respectively. Whether a model with two or one crustal components is preferred, the calculations show that contamination with Precambrian crust accompanying fractional crystallization can account for the Pb isotope variation of the Harrat Rahat suite, but that the amounts of crust assimilated were small.

Source Lithology

Although variation in isotopic compositions is small at the mafic end of the Harrat Rahat suite, there is a substantial range in trace-element ratios. The absolute concentrations of the highly incompatible elements vary by almost a factor of 10 whereas elements like Yb and Lu vary in concentration by only a factor of 5. Here we focus on the variation in trace-element ratios that are minimally affected by fractional crystallization but can indicate either source heterogeneity or variation in degree of melting. Trace-element ratios that are minimally affected by melting processes like Nb/U, Ba/Th, La/Nb show no correlation with isotopic composition (fig. 8) and vary by at least a factor of two. Parent/daughter ratios do not vary systematically with their isotope ratios indicating that the variations are not related to an ancient fractionation process. Therefore, we explore to what degree the trace-element variations could be caused by variation in the degree of melting and conditions of melting.

The mafic magmas either derived from an enriched source with respect to trace elements or from a depleted source that melted to low extents (Sisson and others, 2023). Harrat Rahat basalts have light rare earth element (REE) enrichment, low Zr/ Nb, and relatively high Ba/La similar to shield-stage

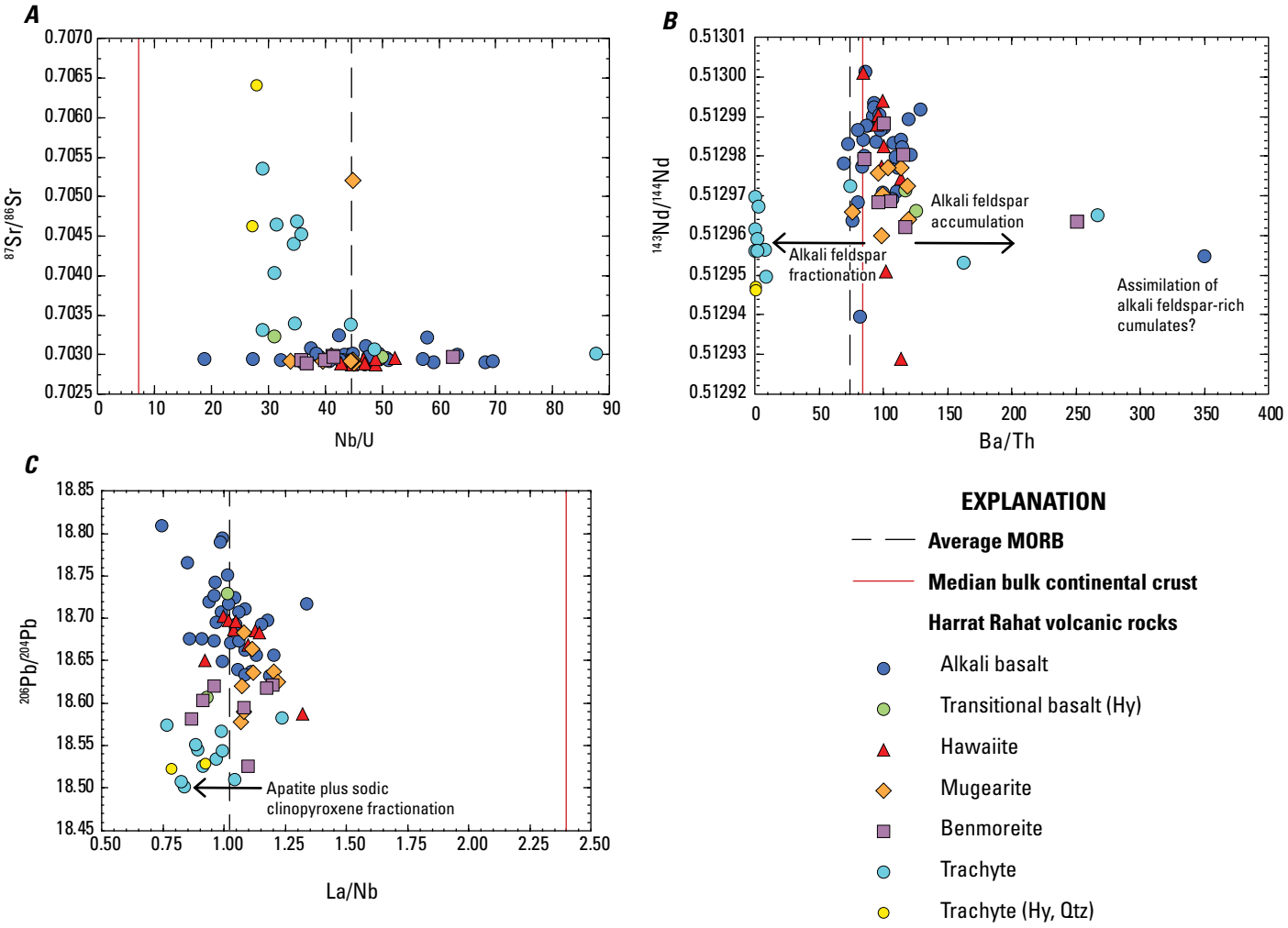

Figure 8. Plots of trace element ratios that are insensitive to degree of melting versus isotopic composition. Vertical lines show ratio values for average midocean ridge basalt (MORB) of Gale and others (2013) and median of estimates for the bulk continental crust of Hacker and others (2015). Arrows show effects of loss or gain of indicated mineral phases during crystallization differentiation.

Hawaiian basalts (fig. 9; Frey and others, 1994; Rhodes, 1996; Yang and others, 1996; Pietruszka and Garcia, 1999; Huang and Frey, 2003). For some Hawaiian basalts, it is argued that their source was not a single lherzolitic lithology, but that a pyroxenitic lithology with roughly gabbroic composition was also present in sufficient abundance to influence melt compositions appreciably (Sobolev and others, 2007). The effect on the magma chemistry of the presence of a pyroxenite lithology in addition to lherzolite has been evaluated by Stracke and Bourdon (2009). Their approach shows that several trace-element ratios would show large differences in behavior depending on whether pyroxenite is present. These ratios include Ba/Nb, Ba/Th, and La/Nb for which the bulk partition coefficient ratios for pyroxenite are higher, and Sr/Pb, Sr/Sm, Sr/Zr, and Zr/Pb for which the bulk partition coefficient ratios for pyroxenite are lower than peridotite. Since plagioclase is a liquidus phase in the Harrat Rahat magmas, ratios that include Sr are compromised by crystal fractionation and are not used. Figure 10 shows Ba/Nb versus Ce/Yb and Zr/Pb and includes mixing calculations of melts derived from pyroxenite and peridotite. As starting composition for the peridotite component, we used bulk silicate earth (BSE) from McDonough and Sun (1995) and for the pyroxenite we used the composition from Stracke and Bourdon (2009), which is calculated as a mixture of recycled MORB and lower continental crust. Since the liquidus temperature of pyroxenite is lower than that of peridotite, we have modeled it as a higher degree melt from pyroxenite. The parameters used in the calculations are listed in table 5. Pyroxenite melting is assumed to be modal. The low Ba/Nb for the range of Ce/Yb values (fig. 9) makes it clear that pyroxenite melts are not a likely cause for the compositional variations of the Harrat Rahat basalts.

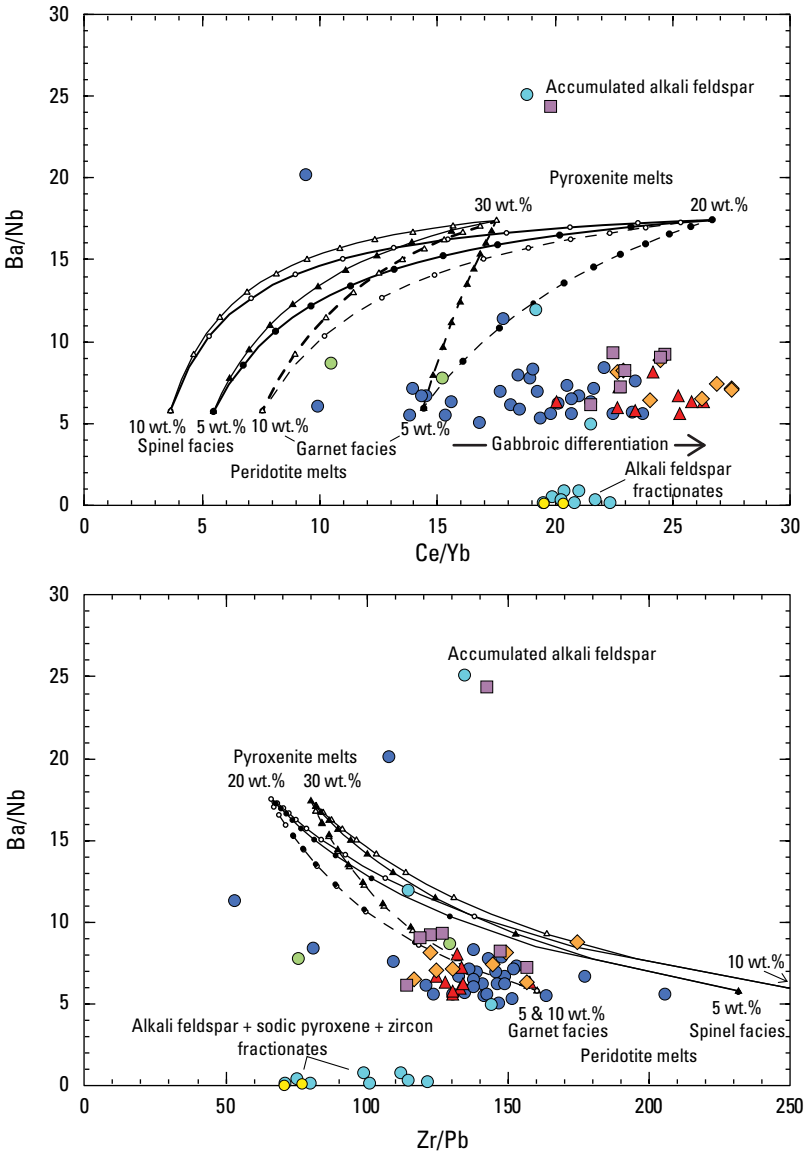

EXPLANATION

Harrat Rahat volcanic rocks

- Alkali basalt
- Transitional basalt (Hy)
- Hawaiite
- Mugearite
- Benmoreite
- Trachyte
- Trachyte (Hy, Qtz)

Figure 9. Plots of trace element ratios that are affected differently by pyroxenite versus peridotite melting. Mixing curves are between partial melts of pyroxenites (high Ba/Nb) with partial melts of garnet peridotite (dashed lines) and spinel peridotite (solid lines). Symbols on curves represent 5 weight percent (wt.%) mixture increments. Curves with open symbols are for 10 weight percent peridotite melts, curves with filled symbols are for 5 weight percent peridotite melts. Circles on curves indicate mixtures with a 20 weight percent melt from pyroxenite and triangles are for mixtures with a 30 weight percent melt of pyroxenite.

Another test of pyroxenite lies in trace element variations with isotopic compositions. As pyroxenites are generally enriched in incompatible elements, radiogenic ingrowth during any significant aging should lead to an enriched signal in their isotopic compositions. Low-degree melts are expected to have a larger complement of pyroxenite melt compared to high-degree melts because of the difference in melting temperatures between pyroxenite and peridotite. Figure 10 shows an example of an incompatible element ratio sensitive to melting, like Zr/Nb, versus Nd isotopic composition, where high Zr/Nb corresponds to a higher degree of melting and thus a higher $^{143}Nd/^{144}Nd$ is expected. However, no correlations are observed. The same can be shown for the Pb, Sr, and Hf isotopic compositions as well as other trace-element ratios such as Ce/Yb and Y/Nb. The absence of systematic variations between isotopic composition and trace-element ratios sensitive to the degree of melting allow us to conclude that pyroxenite played no discernable role in generating the trace-element content and isotope composition variation.

Moufti and others (2012) argued for a two-lithology source for the magmas of northern Harrat Rahat. One lithology was argued to be garnet lherzolite and the second was peridotite that contained amphibole. The presence of amphibole was argued based on positive concentration anomalies for Ba, Nb, Sr, Zr, and Ti on a Coryell-Masuda (spider) diagram. High Nb/Ba and low Rb/Ba were cited as evidence for involvement of a fluid that "extracted" the Rb and increased the Nb concentration in the residue; Ba concentrations were thought to have been buffered by the presence of residual amphibole. This is also argued by Sanfilippo and others (2019) for Harrat Lunayyir and Harrat Khaybar volcanic rocks. Our larger suite of mafic volcanic rocks from northern Harrat Rahat, however, does not show elevated Nb/Ba or low Rb/Ba; the median values are similar to MORB, but the rocks do have positive Ti concentration anomalies on a Coryell-Masuda diagram (fig. 11), which would be expected from amphibole partition coefficients (Tiepolo and others, 2007). Figure 11 only shows the patterns

Table 5. Mantle-source melting parameters.

[Partition coefficients from compilation of Stracke and Bourdon (2009) and references therein except spinel partition coefficients for Nb and Zr, which are from Elkins and others (2008); other spinel partition coefficients are assigned as zero]

	Olivine	Orthopyroxene	Clinopyroxene		Garnet	Spinel	Pyroxenite bulk
			Low Ca	High Ca			
Reactions to produce one mass unit of melt							
2 GPa	0.10	0.20	−1.25	−1.25	0.00	−0.05	–
3 GPa	−0.14	0.72	−1.48	−1.48	−0.10	0.00	–
Initial modal proportions, by mass fraction							
2 GPa	0.53	0.24	0.18	0.18	0.00	0.05	–
3 GPa	0.53	0.08	0.34	0.34	0.05	0.00	–
Partition coefficient (*D*)							
Ba	0.000005	0.000006	0.0004	0.0004	0.00007	0	0.0054
Pb	0.003	0.009	0.009	0.012	0.005	0	0.0420
La	0.0002	0.0031	0.0054	0.03	0.0007	0	0.025
Ce	0.0003	0.004	0.038	0.08	0.017	0	0.049
Sm	0.0011	0.02	0.1509	0.2990	0.23	0	0.26
Nd	0.00042	0.012	0.0884	0.0884	0.064	0	0.15
Dy	0.0027	0.011	0.17	0.4	2	0	0.88
Yb	0.03	0.08	0.25	0.45	5.5	0	2.00
Zr	0.0022	0.03	0.1555	0.2835	0.52	0.008	0.190
Nb	0.0005	0.004	0.03	0.015	0.015	0.0006	0.008

of the most magnesian Harrat Rahat samples and shows that the patterns are similar to those of ocean island basalts, for example, average Mauna Loa shield basalt. If relatively high Nb concentrations are explained as a residue of fluid extraction (Moufti and others, 2012), it conflicts with the elevated Sr concentrations of Harrat Rahat magmas, since Sr is also a fluid-mobile element and would be depleted by fluid extrac-tion, much as proposed for Rb. The most obvious anomaly is in titanium concentrations. However, we have not found a correlation of Ti anomaly (Ti_N/Ti^*, where $Ti^* = [Dy_N+Ho_N]/2$ and subscript N stands for normalization to BSE) with any other parameter in the most mafic samples. The Ti anomaly in the most mafic samples is relatively limited ($Ti_N/Ti^* = 1$ to 2, with an average of about 1.4) and not correlated with isotopic composition (fig. 12). The more evolved samples have very low Ti anomaly values, indicating crystallization of Fe-Ti oxide. Sisson and others (2023) present evidence that many evolved Harrat Rahat basalts and hawaiites re-entrained earlier cumulates from the Cenozoic magmatic system, evident prominently by selective assimilation of cumulus apatite, and our preferred interpretation of the high Ti anomaly is similar re-entrainment of titanomagnetite olivine gabbro cumulates leading to preferential assimilation of Fe-Ti oxides in which the more primitive magmas were undersaturated.

The presence of amphibole residual in the source would also strongly limit the possible pressures and temperatures where magmas could have been generated as well as their H_2O concentrations (Mandler and Grove, 2016). The phenocryst assemblage in the mafic magmas lacks hydrous minerals, and the low thermal (<1,100 degrees Celsius [°C]) and fairly low pressure (<2.4 gigapascals [GPa]) stability field of hydroxy-calcic amphiboles (Gilbert and others, 1982; Foley, 1991), particularly in the presence of orthopyroxene (Lykins and Jenkins, 1992), are difficult to reconcile with the probable high magmatic temperatures suggested by the high MgO concentrations of many harrat basalts, as well as with the probable presence of garnet in the source region. If amphibole were present in the source, it most likely was a trace phase and would not have been residual to melting; therefore, the trace-element characteristics of the magmas do not require a two-lithology source.

Degree of Melting

It first should be noted that the trace-element variations of Harrat Rahat basaltic magmas are relatively limited. Much of their concentration variations result from extensive gabbroic fractional crystallization in the crust (Sisson and others, 2023). The variation in incompatible trace-element ratios at Harrat Rahat are limited compared to other Cenozoic harrat volcanism on the Arabian Shield. Compared to other Arabian harrats, as well as with Hawaiian basalts, the Zr/Nb is relatively high and overlaps with values of Indian Ocean MORB. Ce/Yb of northern Harrat Rahat basalts is at the lower end of the range of other Arabian harrat basalts.

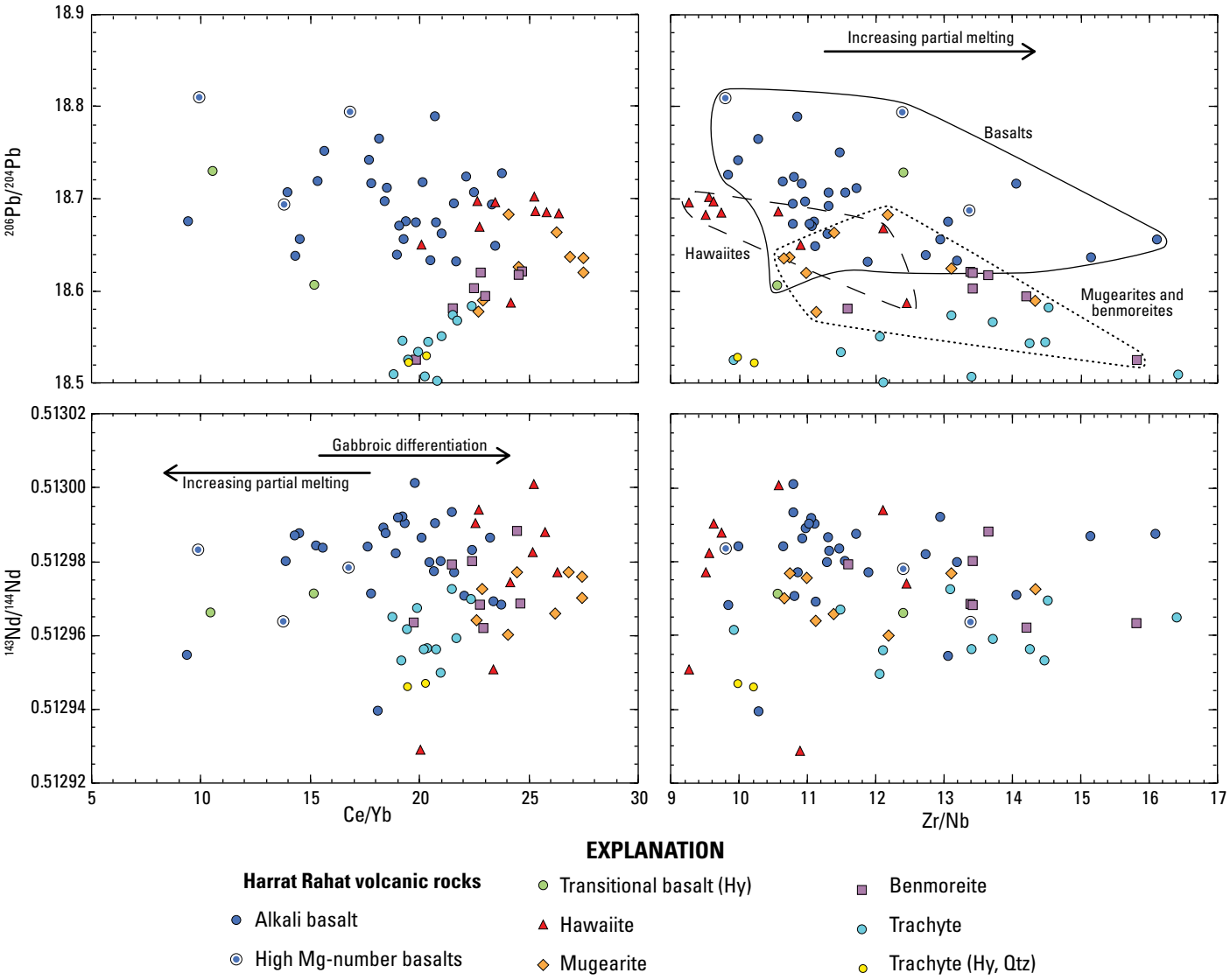

Figure 10. Plots of Pb and Nd isotopic composition versus trace element ratios that are sensitive to degree of melting and to mixing with pyroxenite partial melts. Aged pyroxenites would have low $^{143}Nd/^{144}Nd$ and high $^{206}Pb/^{204}Pb$. Their intermediate-degree partial melts (20–30 weight percent) would have Ce/Yb≤15 whereas low- to moderate-degree partial melts of peridotite (<10 weight percent) would have Ce/Yb≥15, so mixing of peridotite and pyroxenite melts would produce a positive trend of Ce/Yb versus Pb-isotopes and a negative trend versus Nd isotopes. These are not seen in the compositions of Harrat Rahat basalts. The Nb bulk partition coefficient (*D*) is less than that of Zr ($D_{Nb} < D_{Zr}$) for both pyroxenites and peridotites, but the difference is smaller in pyroxenites, so their moderate-degree partial melts generally will have higher Zr/Nb than low-degree melts of peridotite. Mixing of peridotite and pyroxenite partial melts should, therefore, produce a positive array on a plot of Zr/Nb versus $^{206}Pb/^{204}Pb$ and a negative array versus $^{143}Nd/^{144}Nd$. If anything, the reverse is seen in the Pb isotope plot of the Harrat Rahat volcanic rocks, and no obvious trend appears in the Nd isotope plot. These relations indicate that pyroxenite is not a significant contributor to Harrat Rahat magmas.

The Nd and Hf isotopic compositions of the magmas are more radiogenic than BSE and overlap with values of enriched MORB. The Sr isotopic compositions of the mafic magmas are also close to the field for MORB, whereas the Pb isotopic compositions are close to the NHRL, which indicates that the source of the Harrat Rahat volcanism is long-term depleted compared to BSE but somewhat enriched relative to the depleted mantle (DM) end member.

We have modeled REE ratios resulting from melting of a peridotitic composition both with BSE and DM (Salters and Stracke, 2004) bulk compositions, as the isotopic composition of the basalts are more depleted than BSE but less depleted than the source for normal MORB. To investigate the depth of melting, we calculated the compositional trajectories of melts from the garnet and the spinel stability fields (fig. 13 and 14) using a near-fractional melting model with 0.2 percent

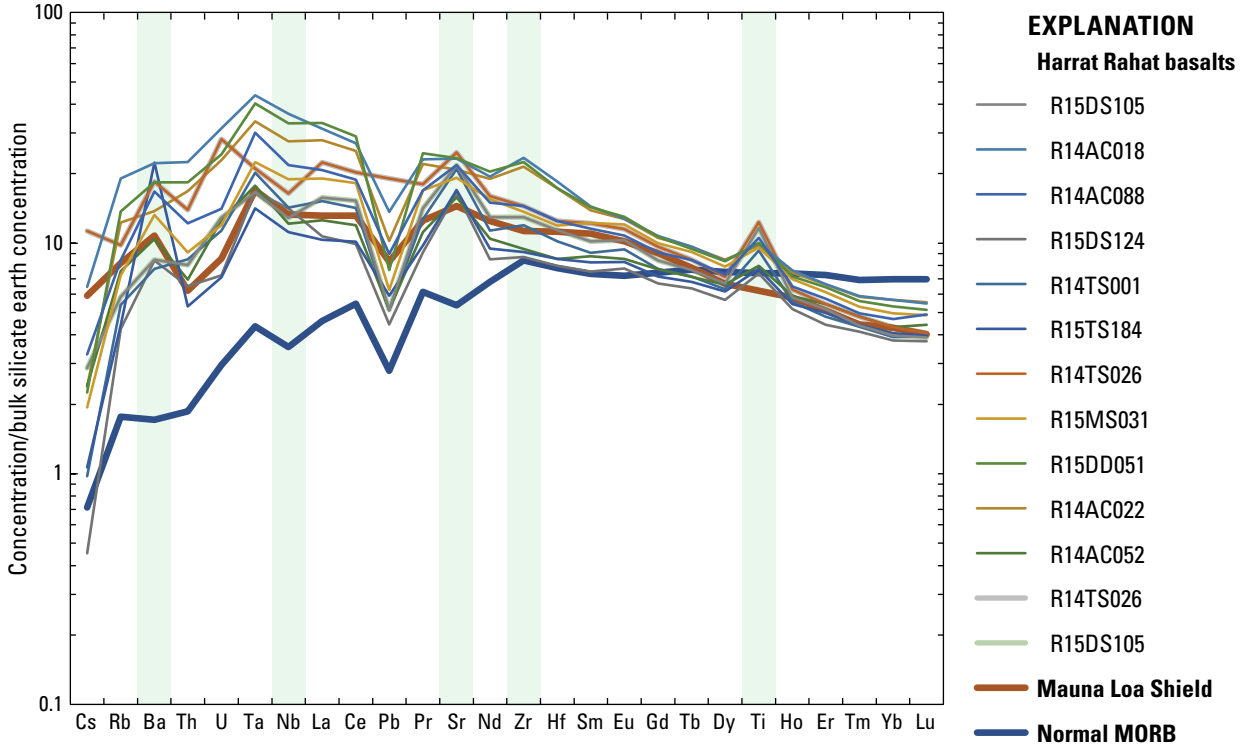

Figure 11. Coryell-Masuda diagram of the 13 most magnesian basalts from Harrat Rahat normalized to bulk silicate earth (McDonough and Sun, 1995). Normal midocean ridge basalt (MORB) (White and Klein, 2014) and average Mauna Loa shield basalt (compiled from the GEOROC database) are shown for comparison.

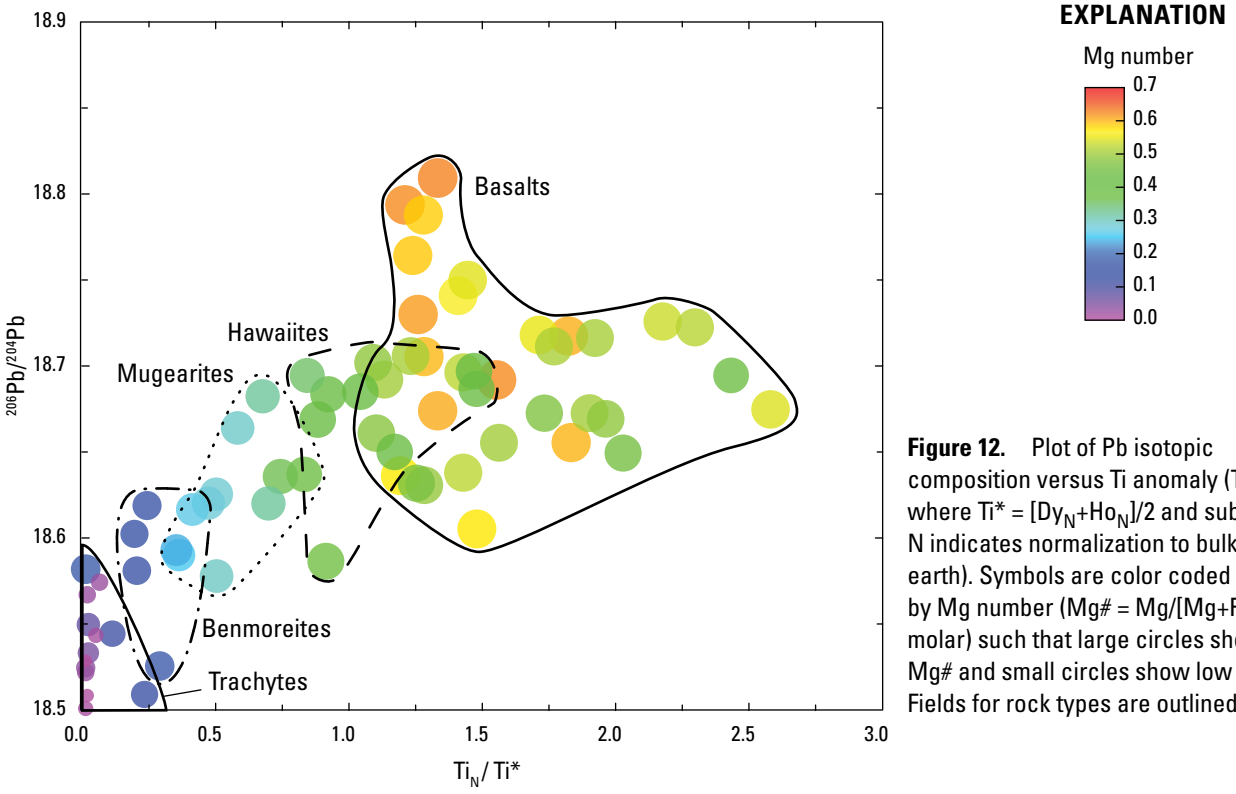

Figure 12. Plot of Pb isotopic composition versus Ti anomaly (Ti_N/Ti^*, where $Ti^* = [Dy_N+Ho_N]/2$ and subscript N indicates normalization to bulk silicate earth). Symbols are color coded and sized by Mg number (Mg# = $Mg/[Mg+Fe^{2+}]$, molar) such that large circles show high Mg# and small circles show low Mg#. Fields for rock types are outlined.

residual porosity. Melts are calculated as extracted in 0.1 weight percent intervals. Spinel peridotite is modeled as having a modal composition and melting reaction at 1.5 GPa (Kinzler and Grove, 1992), and garnet peridotite is modeled with a modal composition and melting reaction appropriate for 2.8 GPa (Longhi, 2002). Apart from the difference in the aluminous mineral present, at 2.8 GPa the garnet peridotite mode would consist of 34 weight percent low-Ca clinopyroxene (8–10 weight percent CaO) and 8 weight percent orthopyroxene. Melting in the garnet stability field consumes low-Ca clinopyroxene, garnet, and olivine, and produces orthopyroxene in addition to melt. At lower pressures, olivine is produced in addition to melt (Longhi, 2002).

As spinel peridotite melting only creates small fractionations in Sm/Yb, melts from the spinel and garnet stability field are clearly separated. Harrat Rahat basalt compositions lie between the two trajectories of melt composition of garnet and spinel peridotite (fig. 13). The high-MgO end of the Harrat Rahat field is close the garnet lherzolite melt trajectory from a BSE source. Compared with other Arabian harrat lavas, Harrat Rahat basalts have some of the highest Dy/Yb (fig. 14) for their La/Yb ratio, indicating a large component of melting of garnet lherzolite. The Dy/Yb and Sm/Yb fractionations are too large to be explained solely by melting at shallow levels in the spinel stability field of a source similar to BSE or more depleted. The heavy REE concentrations in high-Mg# basalts are lower than those in normal MORB (White and Klein, 2014). If one would argue for melting solely in the spinel stability field, and therefore a shallow origin for the magmas, the source would have to have been altered by some recent process that increased Dy/Yb, such as metasomatism by a melt that had garnet in its residue. The isotopic compositions are more depleted than BSE and, consequently, the source has to have had a long-term depleted history. Therefore, the enriched character of the magmas has to be related to a recent process, like low extents of melting. On the basis of the Sm/Yb and Dy/Yb ratios versus La/Sm, where the Harrat Rahat basalt compositions plot between the model calculations for melting in the garnet stability field and the spinel stability field, it is most likely that Harrat Rahat magmas were mainly generated from a garnet lherzolite source, but some melting continued into the spinel field, or some melts that segregated from garnet peridotite continued to react with peridotite short distances into the spinel stability field (fig. 13 and 14). The Harrat Rahat magmas are also offset from seafloor basalts of the active Red Sea rift and Gulf of Aden, both of which are in dominantly extensional tectonic settings where melting extends to shallow levels in the mantle (fig. 13 and 14). Sisson and others (2023) estimate that most Harrat Rahat basalts derived from 2–4 weight percent partial melting of a generally depleted source, or approximately one-third to one-half the extents of melting that yield common MORB.

Further corroborating evidence for relatively deep melting comes from major-element-based estimates of the source temperature and pressure. Generally, such estimates involve computationally reversing the effects of early

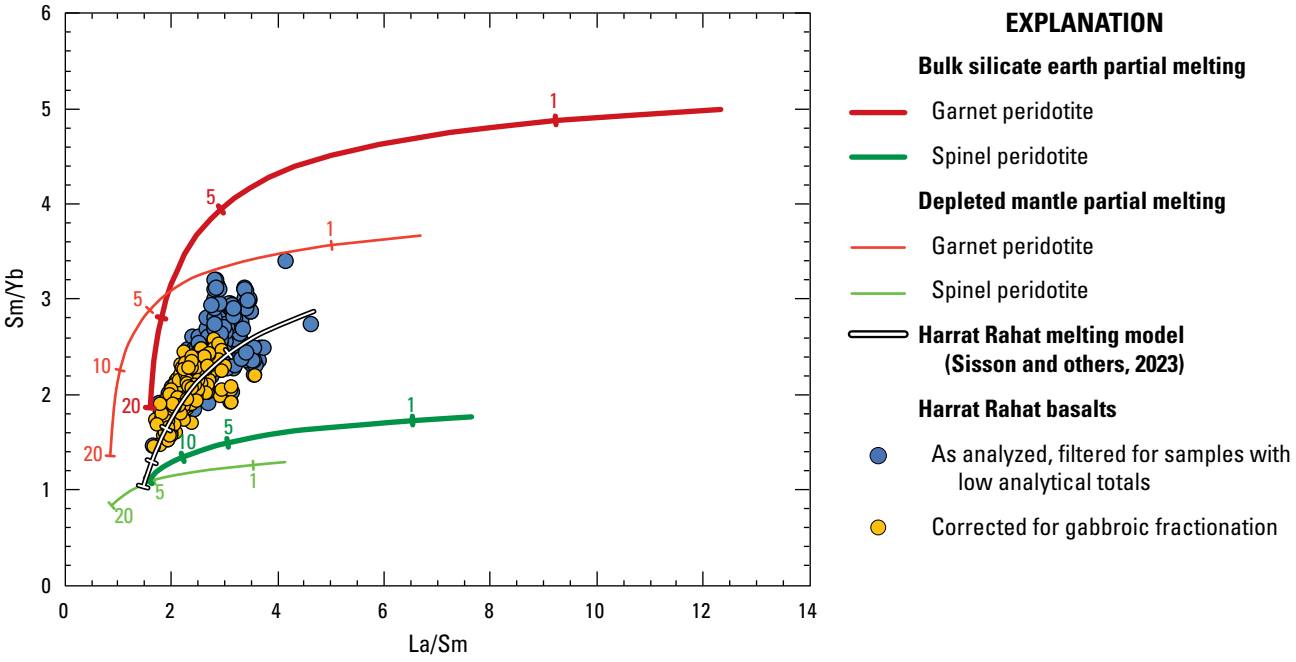

Figure 13. Plot of La/Sm versus Sm/Yb for spinel- and garnet-facies peridotite partial melting compared with Harrat Rahat basalts (blue circles; Downs, 2019) filtered such that MgO ≥6.8 weight percent and P_2O_5/K_2O <0.8 and adjusted to primitive compositions (orange circles) as by Sisson and others (2023). Curves show partial melting behavior of depleted mantle (thin lines) and bulk silicate earth (thick lines) compositions in the garnet (red) and spinel (green) peridotite stability fields. Black and white line shows melting behavior for Harrat Rahat assuming a single set of melting conditions (from Sisson and others, 2023). Melting curves span from 0.1 to 20 weight percent and ticks mark melt fractions of 1, 5, 10, and 20 weight percent.

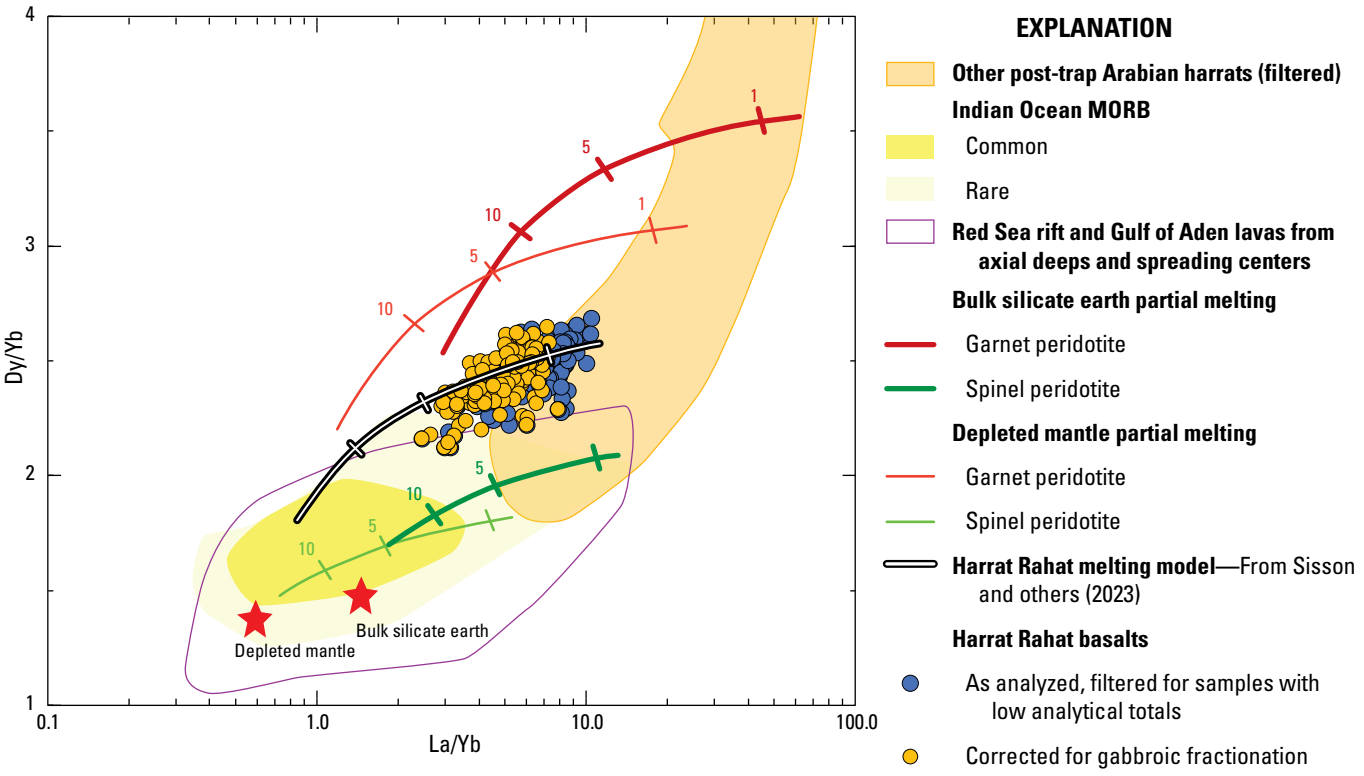

Figure 14. Plot of La/Yb versus Dy/Yb showing a comparison of Harrat Rahat basalts with nearby provinces. The Indian Ocean midocean ridge basalt (MORB) field is subdivided into common versus outlier compositions; other Arabia Plate harrats are filtered to only show rocks with MgO ≥7 weight percent to minimize the effect of crystallization differentiation. Red Sea rift and Gulf of Aden compositions are only samples from submarine deeps, axial troughs, and active islands, excluding subaerial Tertiary rocks that can be altered or that assimilated continental crust. Harrat Rahat basalts (Downs, 2019; blue circles) are filtered such that MgO ≥6.8 weight percent and P_2O_5/K_2O <0.8, and are also shown adjusted to primitive compositions (orange circles) as by Sisson and others (2023). Curves show garnet- and spinel-facies peridotite melting of bulk silicate earth and depleted mantle source compositions, as well as derived for Harrat Rahat assuming a single set of melting conditions (from Sisson and others, 2023). Melting curves span from 0.1 to 20 weight percent and ticks mark melt fractions of 1, 5, and 10 weight percent.

crystallization differentiation to derive melt compositions that match experimentally determined peridotite melting relations and that would be in Fe-Mg equilibrium with an assumed residual olivine composition. As it happens, inferred source temperatures are highly sensitive to the assumed residual olivine composition and oxidation state of the magma. Application of the olivine-addition models of Herzberg and Asimow (2015) or Lee and others (2009) to the least fractionated Harrat Rahat basalts yields source temperature estimates around 1,500 °C and source pressure estimates of 2.4–2.8 GPa, or 80–94 km depth assuming continental thickness of 40 km. These calculations would indicate that the parental magmas were picrites produced in the garnet peridotite stability field that then underwent about 20 weight percent fractionation of olivine before reaching the surface. However, the Herzberg and Asimow (2015) PRIMELT3 model flags the calculated primary magma as too poor in Ca to be in equilibrium with a peridotite source. In contrast, application of the parameterizations of garnet, spinel, and plagioclase peridotite melting of Till and others (2012) and Grove and others (2013) indicate that reversing the effects of 7–8 weight percent olivine fractionation can bring the least fractionated Harrat Rahat basalts into agreement with peridotite melting relations deep in the spinel peridotite stability field (1.8–2.0 GPa, or 62–70 km depth) at source temperature of 1,380–1,405 °C, and that greater additions of olivine fail to match the compositions of garnet peridotite melts (Sisson and others, 2023). A shortcoming of those results is that reversing the effects of no more than 8 weight percent olivine fractionation fails to attain the composition of refractory residual olivine (Mg# = 0.9) commonly employed for models of peridotite melting. Although, assuming that the erupted basalts were moderately oxidized (1 log unit more oxidized than the oxygen fugacity [fO_2] of the quartz-fayalite-magnetite buffer) and that olivine in the source was moderately less refractory (Mg# = 0.889) upon melt segregation can resolve the disparity (Sisson and others, 2023). These cooler temperatures inferred for the Harrat Rahat mantle source agree closely with estimates of the asthenospheric sources for MORB at those depths, and the segregation depths agree with the geophysically imaged shallow lithosphere-asthenosphere boundary beneath the largest harrats (Chang and others, 2011; Yao and others, 2017; Bedrosian and others, 2019). Whichever parental magma estimate is preferred, the inferred source

temperatures greatly exceed the thermal stability of amphibole and would be much hotter than the <1,000 °C temperatures expected at those depths for undisturbed, amagmatic portions of the Neoproterozoic mantle lithosphere of the Arabia Plate (Rolandone and others, 2013).

Mantle Source Composition of Harrat Rahat Volcanic Rocks

An important part of assessing the mantle source of the Harrat Rahat mafic magmas is their isotopic composition. There are several components that are potentially present in the source of the Harrat Rahat magmas. Shaw and others (2003) argued for the presence of a HIMU (high long-term U/Pb; Stracke and others, 2005) component for Arabian Shield magmas and the Afar plume, and Dupal anomaly (Hart, 1984) signatures characteristic of Indian Ocean MORB are also potential components based on geographic proximity. In Sr-Nd isotope space, the mafic Harrat Rahat magmas fall within the compositional range of Indian Ocean MORB. They are offset from basalts of the active Red Sea rift to less radiogenic Nd for a given Sr isotopic composition. Compared with other Arabian harrats, the least evolved Harrat Rahat basalts are among the most radiogenic in Nd isotopic composition, and most other Arabian harrat magmas are also slightly more radiogenic in Sr. There is some overlap with the compositions of magmas associated with the Afar plume, although the composition proposed for the pure Afar plume (fig. 2) is more radiogenic in Sr and less radiogenic in Nd. The Hf and Nd isotopic variations (fig. 3) are consistent with the observations in Sr-Nd isotope space although there are far fewer published Hf isotope results to compare with.

The Pb isotopic compositions of Harrat Rahat volcanic rocks are close to the NHRL (Hart, 1984). Their $^{206}Pb/^{204}Pb$ and $^{207}Pb/^{204}Pb$ values directly overlap the NHRL, whereas their $^{208}Pb/^{204}Pb$ values are displaced only slightly above it (fig. 4) within the spectrum of Northern Hemisphere oceanic spreading-ridge basalts that were used to define the reference line. Although the range in compositions is limited, the most mafic Harrat Rahat magmas have the most radiogenic Pb compositions, and with evolution to trachytes, the Pb isotopic values shift progressively down the NHRL to less radiogenic values. Pb isotopic values of Harrat Rahat basalts are near the high $^{206}Pb/^{204}Pb$ end of the range of Indian Ocean MORB, but plot along its lower $^{208}Pb/^{204}Pb$ and $^{207}Pb/^{204}Pb$ edges. Collectively, young basalts from the active spreading systems of the Red Sea rift and Gulf of Aden continue the elevated $^{208}Pb/^{204}Pb$ field of Indian Ocean MORB to higher $^{206}Pb/^{204}Pb$ values, whereas Harrat Rahat basalts have lower $^{208}Pb/^{204}Pb$ values, closer to the NHRL and only marginally overlapping the field defined by the active spreading systems that bound the Arabia Plate. Excepting post-trap mafic magmas from Yemen, mafic magmas from other Arabia Plate harrats mostly have higher $^{206}Pb/^{204}Pb$ than those of Harrat Rahat and plot farther above the NHRL, distinctly so in $^{207}Pb/^{204}Pb$. Post-trap mafic lavas from Yemen have similar to lower $^{206}Pb/^{204}Pb$ values than Harrat Rahat basalts and are distinctly above the NHRL in both $^{208}Pb/^{204}Pb$ and $^{207}Pb/^{204}Pb$, and overlap the high $^{206}Pb/^{204}Pb$ end of the field of Indian Ocean MORB. Harrat Rahat Pb isotopic compositions also plot on the edge of the field of magmas whose source is thought to be affected by the Afar plume. The Afar plume composition itself is more radiogenic in Pb (Rooney and others, 2012). The high $^{207}Pb/^{204}Pb$ isotopic compositions of some Red Sea rift basalts have been attributed to a component from the continental lithosphere (Eissen and others, 1989). Compositions that plot significantly above the NHRL are considered to contain a sub-continental lithosphere component (Schilling and others, 1992; Bertrand and others, 2003). Direct determinations are few for the Arabian-Nubian lithospheric mantle, but massif peridotites from Jazīrat Zabarjad (Saint Johns Island or Zabargad Island) (Brueckner and others, 1995) and peridotite xenoliths from Jordan (Shaw and others, 2007) have $^{207}Pb/^{204}Pb$ values reaching to appreciably greater than the NHRL at $^{206}Pb/^{204}Pb$ values similar to Harrat Rahat (fig. 4), consistent with high $^{207}Pb/^{204}Pb$ characterizing portions of the Arabia Plate sub-continental mantle lithosphere. In contrast, the NHRL-like Pb isotopic compositions of Harrat Rahat magmas indicates there is little influence of sub-continental lithosphere.

The location of the suite in the Pb-Pb isotope diagram (fig. 4), as well as in Sr-Nd isotope space (fig. 2), indicates that the Harrat Rahat basalts can be explained as deriving from a mixture of depleted Northern Hemisphere asthenosphere with a component that has a more radiogenic Pb isotopic composition and lies near the NHRL, is more radiogenic in Sr, and is less radiogenic in Nd. The proposed Afar plume composition clearly fits these requirements. A more extreme composition would be the HIMU end member (Stracke and others, 2005), as that proposed composition has $^{206}Pb/^{204}Pb$ of 21.5 and is on or just under the NHRL. An Afar plume component was argued for the post-trap volcanic field near Ṣan‘ā’, Yemen (Baker and others, 1997), as a contaminant in depleted MORB-type mantle. The Ṣan‘ā’ rocks’ Pb isotopic compositions extend to higher $^{206}Pb/^{204}Pb$ than those of Harrat Rahat, which is expected as they are closer to the Afar plume center. In Pb-Nd isotope space (fig. 6), the Harrat Rahat volcanic rocks also plot between an asthenospheric composition and an Afar plume-like component. However, the asthenospheric component is not similar to Indian Ocean MORB, which have elevated $^{207}Pb/^{204}Pb$ and $^{208}Pb/^{204}Pb$ for a given $^{206}Pb/^{204}Pb$ value—that is, they plot well above the NHRL (Dupré and Allègre, 1983; Hamelin and Allègre, 1985). This is illustrated in figure 15 that plots the deviation from the NHRL as proposed by Hart (1984), where Indian Ocean MORB has clear positive $\Delta^{208}Pb/^{204}Pb$ and $\Delta^{207}Pb/^{204}Pb$. Therefore, Indian Ocean asthenosphere cannot be present in the source of Harrat Rahat basalts. The only potential source is depleted asthenospheric mantle similar to that beneath and fueling the Atlantic and Pacific Ocean volcanic spreading ridges.

The Harrat Rahat volcanic field stands out by its limited diversity in isotopic composition compared to some of

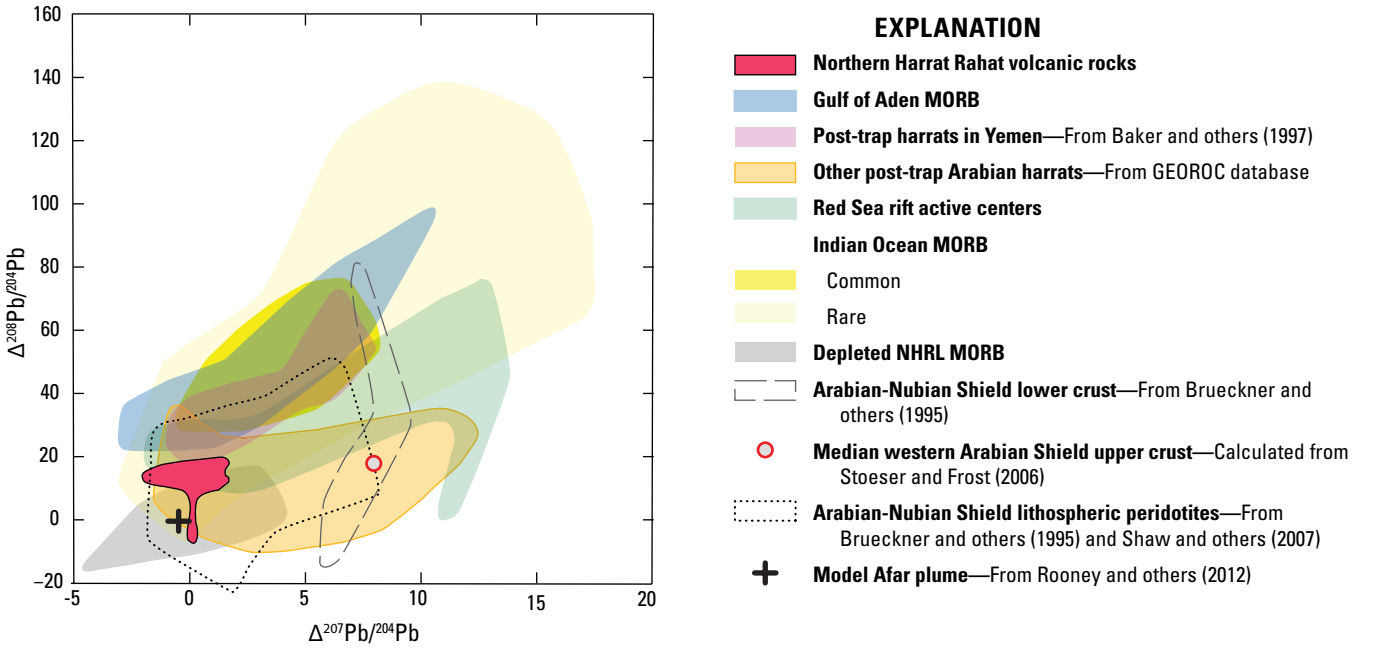

Figure 15. Plot of $\Delta^{207}Pb/^{204}Pb$ versus $\Delta^{208}Pb/^{204}Pb$ of Harrat Rahat volcanic rocks compared with other provinces, where Δ refers to the deviation from the Northern Hemisphere Reference Line (NHRL) (Hart, 1984). Strongly depleted Atlantic and Pacific Ocean midocean ridge basalts (MORB) cluster near $\Delta^{207}Pb/^{204}Pb = 0\pm5$ and $\Delta^{208}Pb/^{204}Pb = 0\pm20$ (gray area), whereas combined pronounced deviations to positive $\Delta^{208}Pb/^{204}Pb$ and $\Delta^{207}Pb/^{204}Pb$ shown by Indian Ocean MORB are manifestations of the Dupal mantle geochemical anomaly (Hart, 1984). Similar deviations of Gulf of Aden MORB and post-trap harrat rocks from Yemen can be attributed to substantial asthenospheric mantle in their magmatic sources that has Dupal-anomaly compositions. Sub-continental mantle lithosphere ranges from the origin to higher $\Delta^{207}Pb/^{204}Pb$ than $\Delta^{208}Pb/^{204}Pb$. Arabia Plate harrat rocks from north of Yemen generally show this shift to higher $\Delta^{207}Pb/^{204}Pb$ that can be interpreted as caused by interaction with the sub-continental mantle lithosphere. Basalts from the active Red Sea rift system define a trend intermediate between the strong Dupal anomaly and mantle lithosphere effects, consistent with some influence by both components. Harrat Rahat isotopic compositions cluster at the low $\Delta^{207}Pb/^{204}Pb$ and $\Delta^{208}Pb/^{204}Pb$ end of the field of Arabian harrats, close to the approximate field of depleted Northern Hemisphere MORB, consistent with small or no discernable contributions from either Dupal-anomaly asthenosphere or sub-continental mantle lithosphere. Approximate field of depleted NHRL MORB is defined by the greatest clustering of determinations for basalts from the East Pacific Rise and Mid-Atlantic Ridge filtered for $^{87}Sr/^{86}Sr < 0.7030$ (compiled from the PetDB database). Gulf of Aden, Red Sea rift, and Indian Ocean MORB values compiled from the PetDB database, excluding Tertiary Red Sea rift rocks exposed along the Arabian continental margin and Jazīrat Zabarjad, which are influenced by crustal assimilation and alteration.

the other harrats. Harrat Rahat magmas have significantly lower $\Delta^{208}Pb/^{204}Pb$ than other investigated harrats. The higher $\Delta^{208}Pb/^{204}Pb$ of the other harrats can be explained by contamination with a continental lithosphere component (Baker and others, 1997), and Harrat Rahat is unique in that it does not show this influence. Harrat Rahat is the largest of the Neogene–Quaternary harrats atop the exposed Arabian Shield, and it overlies the shallowest depth to the lithosphere-asthenosphere boundary (Chang and others, 2011; Yao and others, 2017; Bedrosian and others, 2019), both factors potentially reducing lithospheric interaction. There are several comparisons that can be made with other volcanic fields or provinces. Compared to other recent volcanism on the Arabian Peninsula, the Harrat Rahat volcanic field is restricted in composition and plots at the unradiogenic Sr (fig 2) and Pb (fig. 4) end of the Arabian volcanic province toward MORB-like compositions; it is, in effect, the most similar among the Arabian harrats to Northern Hemisphere MORB in its isotopic characteristics.

We performed simple melt mixing calculations between average normal MORB (White and Klein, 2014) and the Afar plume isotopic composition of Rooney and others (2012) to which we assigned trace-element concentrations of average mafic magmas of the Afar province. Those calculations show that the Harrat Rahat Pb, Sr, and Nd isotopic compositions are consistent with about 20–30 weight percent Afar plume melts combined with normal MORB. Mixing of the mantle source, rather than of melts, is more consistent with the isotopic

homogeneity of Harrat Rahat basalts, but modeling source mixing requires additional uncertain assumptions, and the results are not expected to differ greatly from the simple melt-mixing approximation.

The Harrat Rahat results thus indicate a source that is consistent with the model of Ebinger and Sleep (1998), Chang and others (2011), and Yao and others (2017) where some material from the Afar plume has channeled under the western part of the Arabian Shield, resulting in uplift by removal of the lower lithosphere and triggering volcanism that constructed the harrats, although the dominant material undergoing melting to fuel Harrat Rahat is ordinary depleted asthenosphere mixed with subordinate Afar plume. It is unknown whether this dominant depleted upper mantle asthenosphere was entrained and brought into motion along the ascending plume's margin, was displaced by the spreading plume, or was in some other way triggered into enhanced convective circulation and partial melting. Our study shows that the amount of lithospheric contamination is minimal for Harrat Rahat as that would result in a deviation from NHRL. This absence of lithospheric contamination seems to be unique for the volcanic field and probably reflects the minimum thickness of mantle lithosphere beneath the harrat as well as its relatively high magmatic flux.

Conclusions

Harrat Rahat magmas come from a relatively homogeneous mantle source, and their correlation between Pb isotopic composition and Mg# indicates that contamination with Precambrian continental materials was progressive with differentiation but minor in absolute amount, estimated at approximately 5 weight percent in aggregate across the entire basalt to trachyte spectrum. The evolved trachytic rocks (Mg# <0.1) show a pronounced upper crustal contamination signal owing to their low Sr concentrations and the high $^{87}Sr/^{86}Sr$ values of some rocks of the Arabian Shield.

Trace-element variations, in combination with isotopic compositions, indicate that magmas derived from a single peridotitic lithology, and variations in incompatible trace elements can be related to variations in the degree of melting and not source composition. A substantial part of the melting took place in the garnet stability field.

The magma compositions are consistent with a source that is a combination of predominantly depleted mantle (Salters and Stracke, 2004) and subordinate Afar plume (Rooney and others, 2012). The depleted mantle component is similar to the Atlantic or Pacific MORB source, and Indian Ocean asthenosphere is absent in the Harrat Rahat source. In addition, a sub-continental lithosphere component that is interpreted for other smaller and less active Arabian harrats is absent in the Harrat Rahat source probably because of the thinness of the mantle lithosphere beneath the volcanic field combined with its relatively high flux of magmas from the asthenosphere.

Acknowledgments

Jorge Vazquez and Andrew Calvert are thanked for their thoughtful reviews of the manuscript. Samples were processed and measured for isotopic values at the National High Magnetic Field Laboratory, which is supported by the National Science Foundation under Cooperative Agreement no. DMR–1157490 and DMR–1644779 and the State of Florida. Collections of samples and analytical expenses were supported through the joint project of the Saudi Geological Survey and the U.S. Geological Survey to study active volcanism near Al Madīnah. That project was possible through the vision and leadership of Dr. Zohair Nawab, Saudi Geological Survey President (retired), and the management of Dr. Hani Zahran, former Director of the (Saudi) National Centre for Earthquakes and Volcanoes. The manuscript was skillfully edited by Dr. Monica Erdman.

References Cited

Altherr, R., Henjes-Kunst, F., and Bauman, A., 1990, Asthenosphere versus lithosphere as possible sources for basaltic 0p2

Baker, J.A., Menzies, M.A., Thirwall, M.F., and Macpherson, C.G., 1997, Petrogenesis of Quaternary intraplate volcanism, Sana'a, Yemen—Implications for plume-lithosphere interaction and polybaric melt hybridization: Journal of Petrology, v. 39, p. 1359–1390.

Bedrosian, P.A., Peacock, J.R., Dhary, M., Sharif, A., Feucht, D.W., and Zahran, H., 2019, Crustal magmatism and anisotropy beneath the Arabian shield—A cautionary tale: Journal of Geophysical Research, v. 124, p. 10153–10179.

Bertrand, H., Chazot, G., Blichert-Toft, J., and Thoral, S., 2003, Implications of widespread high-mu volcanism on the Arabian Plate for Afar mantle plume and lithosphere composition: Chemical Geology, v. 198, p. 47–61.

Blusztajn, J., Hart, S.R., Shimizu, N., and McGuire, A.V., 1995, Trace-element and isotopic characteristics of spinel peridotite xeonliths from Saudi Arabia: Chemical Geology, v. 123, p. 53–65.

Bohannon, R.G., Naeser, D.L., Schmidt, D.L., Zimmermann, R.A., 1989, The timing of uplift, volcanism, and rifting peripheral to the Red Sea—A case for passive rifting?: Journal of Geophysical Research, v. 94, p. 1683–1701.

Bosworth, W., 2015, Geological evolution of the Red Sea—Historical background, review, and synthesis, in N.M.A. Rasul, N.M.A., and Stewart, I.C.F., eds., The Red Sea: Springer-Verlag, Berlin, p. 45–78.

Brueckner, H., Elhadad, M.A., Hamelin, B., Hemming, S., Kroner, A., Reisberg, L., and Seyler, M., 1995, A Pan African origin and uplift for the gneisses and peridotites of Zabargad Island, Red Sea—A Nd, Sr, Pb, and Os isotope study: Journal of Geophysical Research, v. 100, p. 22283–22297.

Brueckner, H., Zindler, A., Seyler, M., and Bonatti, E., 1988, Zabargad and the isotopic evolution of the sub-Red Sea mantle and crust: Tectonophysics, v. 150, p. 163–176.

Calvert, A.T., and Sisson, T.W., 2023, Cenozoic tectonics of the western Arabia Plate related to harrat magmtism near Al Madīnah, Kingdom of Saudi Arabia, chap. B *of* Sisson, T.W., Calvert, A.T., and Mooney, W.D., eds., Active volcanism on the Arabian Shield—Geology, volcanology, and geophysics of northern Harrat Rahat and vicinity, Kingdom of Saudi Arabia: U.S. Geological Survey Professional Paper 1862 [also released as Saudi Geological Survey Special Report SGS–SP–2021–1], 28 p., https://doi.org/10.3133/pp1862B.

Camp, V.E., Hooper, P.R., Roobol, J.M., and White, D.L., 1987, The Madinah eruption, Saudi Arabia—Magma mixing and simultaneous extrusion of three basaltic chemical types: Bulletin of Volcanology, v. 49, p. 489–508.

Camp, V.E., and Roobol, M.J., 1989, The Arabian continental alkali basalt province; Part I—Evolution of Harrat Rahat, Kingdom of Saudi Arabia: Geological Society of America Bulletin, v. 101, p. 71–85.

Camp, V.E., Roobol, M.J., 1991, Geologic map of the Cenozoic Harrat Rahat lava field, Kingdom of Saudi Arabia: Saudi Arabian Deputy Ministry for Mineral Resources Geoscience Map GM-123, scale 1:250,000, 37 p.

Camp, V.E., and Roobol, M.J., 1992, Upwelling asthenosphere beneath western Arabia and its regional implications: Journal of Geophysical Research, v. 97, p. 15255–15271.

Camp, V.E., Roobol, M.J., and Hooper, P.R., 1991, The Arabian continental alkali basalt province; Part II—Evolution of Harrats Khaybar, Ithnayn, and Kura, Kingdom of Saudi Arabia: Geological Society of America Bulletin, v. 103, p. 363–393.

Camp, V.E., Roobol, M.J., and Hooper, P.R., 1992, The Arabian continental alkali basalt province; Part III—Evolution of Harrat Kishb, Kingdom of Saudi Arabia: Geological Society of America Bulletin, v. 104, p. 379–386.

Chang, S-J., Merino, M., Van der Lee, S., Stein, S., and Stein, C.A., 2011, Mantle flow beneath Arabia offset from the opening Red Sea: Geophysical Research Letters, v. 38, no. L04301, https://doi.org/10.1029/2010GL045852.

Coleman, R.G., 1993, Geologic evolution of the Red Sea: Oxford Monographs on Geology and Geophysics, v. 34, 186 p.

Coleman, R.G., Gregory, R.T., and Brown, G.F., 1983, Cenozoic volcanic rocks of Saudi Arabia: U.S. Geological Survey Open-File Report 83-788, 82 p.

Cox, K.G., Bell, J.D., and Pankhurst, R.J., 1979, The interpretation of igneous rocks: London, George Allen and Unwin, 450 p.

DePaolo, D.J., 1981, Trace element and isotopic effects of combined wallrock assimilation and fractional crystallization: Earth and Planetary Science Letters, v. 53, p. 189–202.

Downs, D.T., 2019, Major- and trace-element chemical analyses of rocks from the northern Harrat Rahat volcanic field and surrounding area, Kingdom of Saudi Arabia: U.S. Geological Survey data release, https://doi.org/10.5066/P91HL91C.

Duncan, R.A., and Al-Amri, A.M., 2013, Timing and composition of volcanic activity at Harrat Lunayyir, western Saudi Arabia: Journal of Volcanology and Geothermal Research, v. 260, p. 103–116.

Dupré, B., and Allègre, C.J., 1983, Pb-Sr isotope variation in Indian Ocean and mixing phenomena: Nature, v. 303, p. 142–146.

Ebinger, C.J., and Sleep, N.H., 1998, Cenozoic magmatism throughout east Africa resulting from impact of a single plume: Nature. v. 395, p. 788–791.

Eissen, J.P., Juteau, T., Joron, J.L., Dupré, B., Humler, E., and Al'Mukhamedov, A., 1989, Petrology and geochemistry of basalts from the Red Sea axial rift at 18° north: Journal of Petrology, v. 30, p. 791–839.

Elkins, L., Gaetani, G., and Sims, K., 2008, Partitioning of U and Th during garnet pyroxenite partial melting—Constraints on the source of alkaline ocean island basalts: Earth and Planetary Science Letters, v. 265, p. 270–286.

Foley, S., 1991, High-pressure stability of the fluor- and hydroxy-endmembers of pargasite and K-richterite: Geochimica et Cosmochimica Acta, v. 55, p. 2689–2694.

Frey, F.A., Garcia, M.O., and Roden., M., 1994, Geochemical characteristics of Koolau Volcano—Implications of inter-shield geochemical differences among Hawaiian volcanoes: Geochimica et Cosmochimica Acta, v. 58, p. 1441–1462.

Gale, A., Dalton, C.A., Langmuir, C.H., Su, Y., and Schilling, J.-G., 2013, The mean composition of ocean ridge basalts: Geochemistry, Geophysics, Geosystems, v. 14, p. 489–518, https://doi.org/10.1029/2012GC004334.

Gilbert, M.C., Helz, R.T., Popp, R.K., and Spear, F.S., 1982, Experimental studies of amphibole stability, *in* Veblen, D.R., and Ribbee, P.H., eds., Amphiboles—Petrology and experimental phase equilibria: Reviews in Mineralogy, v. 9B, p. 229–354.

Grove, T.L., Holbig, E.S., Barr, J.A., Till, C.B., and Krawczynski, M.J., 2013, Melts of garnet lherzolite—Experiments, models and comparison to melts of pyroxenite and carbonated lherzolite: Contributions to Mineralogy and Petrology, v. 166, p. 887–910.

Hacker, B.R., Kelemen, P.B., and Behn, M.D., 2015, Continental lower crust: Annual Reviews of Earth and Planetary Sciences, v. 43, p. 167–205.

Hamelin, B., and Allègre, C.J., 1985, Large-scale regional units in the depleted upper mantle revealed by an isotope study of the South-West Indian Ridge: Nature, v. 315 p. 196–199.

Hart, S.R., 1984, A large scale isotopic mantle anomaly in the Southern Hemisphere: Nature, v. 309, p. 753–757.

Herzberg, C., and Asimow, P.D., 2015, PRIMELT3 MEGA. XLSM software for primary magma calculation—Peridotite primary magma MgO contents from the liquidus to the solidus: Geochemistry, Geophysics, Geosystems, v. 16, p. 563–578.

Huang, S., and Frey, F.A., 2003, Trace element abundances of Mauna Kea basalt from phase 2 of the Hawaii Scientific Drilling Project—Petrogenetic implications of correlations with major element content and isotopic ratios: Geochemistry, Geophysics, Geosystems, v. 4, 8711, 43 p., https://doi.org/10.1029/2002GC000322.

Kinzler, R.J., and Grove, T.L., 1992, Primary magmas of mid-ocean ridge basalts; Part 1—Experiments and methods: Journal of Geophysical Research, v. 97, p. 6885–6906.

Lee, C-T.A., Luffi, P., Plank, T., Dalton, H., and Leeman, W.P., 2009, Constraints on the depths and temperatures of basaltic magma generation on Earth and other terrestrial planets using new thermobarometers for mafic magmas: Earth and Planetary Science Letters, v. 279, p. 20–33.

Longhi, J., 2002, Some phase equilibria systematics of lherzolite melting—1: Geochemistry, Geophysics, Geosystems, v. 3, 33 p., https://doi.org/10.1029/2001GC000204.

Lykins, R.W., and Jenkins, D.M., 1992, Experimental determination of pargasite stability relations in the presence of orthopyroxene: Contributions to Mineralogy and Petrology, v. 112, p. 405–413.

Mandler, B.E., and Grove, T.L., 2016, Controls on the stability and composition of amphibole in the Earth's mantle: Contributions to Mineralogy and Petrology, v. 171, 68 p., https://doi.org/10.1007/s00410-016-1281-5.

McDonough, W.F., and Sun, S-S., 1995, The composition of the Earth: Chemical Geology, v. 120, p. 223–253.

McGuire, A.V., and Stern, R.J., 1993, Granulite xenoliths from western Saudi Arabia—The lower crust of the late Precambria Arabian-Nubian shield: Contributions to Mineralogy and Petrology, v. 114, p. 395–408.

Moufti, M.R.H., 1985, The geology of Harrat Al Madinah volcanic field, Harrat Rahat, Saudi Arabia: University of Lancaster, U.K., Ph.D. thesis, 476 p.

Moufti, M.R., Moghazi, A., and Ali, K.A., 2012, Geochemistry and Sr–Nd–Pb isotopic composition of the Harrat Al-Madinah Volcanic Field, Saudi Arabia: Gondwana Research, v. 21, p. 670–689.

Murcia, H., Lindsay, J.M., Németh, K., Smith, I.E.M., Cronin, S.J., Moufti, M.R.H., El-Masry, N.N., and Niedermann, S., 2016, Geology and geochemistry of late Quaternary volcanism in northern Harrat Rahat, Kingdom of Saudi Arabia—Implications for eruption dynamics, regional stratigraphy, and magma evolution, *in* Németh, K., Carrasco-Núñez, G., Aranda-Gómez, J.J., and Smith, I.E.M., eds., Monogenetic volcanism: Geological Society of London Special Publication 446, p. 173–204, https://doi.org/10.1144/SP446.2.

Pietruszka, A.J., and Garcia, M.O., 1999, A rapid fluctuation in the mantle source and melting history of Kilauea Volcano inferred from the geochemsitry of its historical summit lavas (1790–1982): Journal of Petrology, v. 40, p. 1321–1342.

Reilinger, R., McClusky, S., and ArRajehi, A., 2015, Geodetic constraints on the geodynamic evolution of the Red Sea, *in* Rasul, N.M.A., and Stewart, I.C.F., eds., The Red Sea: Springer-Verlag, Berlin, p. 135–149.

Rhodes, J.M., 1996, Geochemical stratigraphy of lava flows sampled by the Hawaiian Scientific Drilling Project: Journal of Geophysical Research, v. 101, p. 11729–11746.

Robinson, F.A., Foden, J.D., Collins, A.S., and Payne, J.L., 2014, Arabian shield magmatic cycles and their relationship with Gondwana assembly—Insights from zircon U–Pb and Hf isotopes: Earth and Planetary Science Letters, v. 408, p. 207–225.

Rolandone, F., Lucazeau, F., Leroy, S., Mareschal J-C., Jorand, R., Goutorbe, B., and Bouquerel, H., 2013, New heat flow measurement in Oman and the thermal state of the Arabian Shield and Platform: Tectonophysics, v. 589, p. 77–89.

Rooney, T.O., Hanan, B.B., Graham, D.W., Furman, T., Blichert-Toft, J., and Schilling, J.-G., 2012, Upper mantle pollution during Afar plume-continental rift interaction: Journal of Petrology, v. 53, p. 365–389.

Rudnick, R., and Gao, S., 2014, Composition of the continental crust, chap. 4.1 *of* Turekian, K., and Holland, H., eds., Treatise on Geochemistry (2d ed.): Elsevier, v. 4, p. 1–51.

Salters, V.J.M., and Sisson, T.W., 2023, Isotopic compositions (Sr, Nd, Hf, Pb) of Quaternary volcanic rocks of northern Harrat Rahat, Kingdom of Saudi Arabia: U.S. Geological Survey data release, https://doi.org/10.5066/P9FOBQNK.

Salters, V.J.M., and Stracke, A., 2004, The composition of the depleted mantle: Geochemistry, Geophysics, Geosystems, v. 5, no. Q05B07, https://doi.org/10.1029/2003GC000597.

Sanfilippo, A., Cai, Y., Gouveia Jacome., A.P., and Ligi, M., 2019, Geochemistry of Lunayyir and Khaybar volcanic fields (Saudi Arabia)—Insights into the origin of Cenozoic Arabian Volcanism, *in* Rasul, N.M.A., and Stewart, I.C.F., eds., Geological setting, palaeoenvironment and archaeology of the Red Sea: Springer-Verlag, p. 389–415.

Schilling, J.-G., Kingsley, R.H., Hanan, B.B., and McCully, B.L., 1992, Nd-Sr-Pb isotopic variations along the Gulf of Aden—Evidence for Afar mantle plume-continental lithosphere interaction: Journal of Geophysical Research, v. 97, p. 10927–10966.

Shaw, J.E., Baker, J.A., Kent, A.J.R., Ibrahim, K.M., and Menzies, M.A., 2007, The geochemistry of the Arabian lithospheric mantle—A source for intraplate volcanism?: Journal of Petrology, v. 48, p. 1494–1512.

Shaw, J.E., Baker, J.A., Menzies, M.A., Thirlwall, M.F., and Ibrahims, K.M., 2003, Petrogenesis of the largest intraplate volcanic field on the Arabian Plate (Jordan)—A mixed litosphere-asthenosphere source activated by lithospheric extension: Journal of Petrology, v. 44, p. 1657–1679.

Sisson, T.W., Downs, D.T., Calvert, A.T., Dietterich, H.R., Mahood, G.A., Salters, V.J.M., Stelten, M.E., and Shawali, J., 2023, Mantle origin and crustal differentiation of basalts and hawaiites of northern Harrat Rahat, Kingdom of Saudi Arabia, chap. I *of* Sisson, T.W., Calvert, A.T., and Mooney, W.D., eds., Active volcanism on the Arabian shield—Geology, volcanology, and geophysics of northern Harrat Rahat and vicinity, Kingdom of Saudi Arabia: U.S. Geological Survey Professional Paper 1862 [also released as Saudi Geological Survey Special Report SGS–SP–2021–1], 42 p., https://doi.org/10.3133/pp1862I.

Sobolev, A.V., Hofmann, A.W., Kuzmin, D.V., Yaxley, G.M., Arndt, N.T., Chung, S.-L., Danyushevsky, L.V., Elliott, T., Frey, F.A., Garcia, M.O., Gurenko, A.A., Kamenetsky, V.S., Kerr, A.C., Krivolutskaya, N.A., Matvienkov, V.V., Nikogosian, I.K., Rocholl, A., Sigurdsson, I.A., Sushchevskaya, N.M., and Teklay, M., 2007, The amount of recycled crust in the source of mante-derived basalts: Science, v. 316, p. 412–417, https://doi.org/10.1126/science.%201138113.

Stein, M., and Goldstein, S.L., 1996, From plume head to continental lithosphere in the Arabian-Nubian shield: Nature, v. 382, p. 773–778.

Stein, M., and Hofmann, A.W., 1992, Fossil plume head beneath the Arabian lithosphere?: Earth and Planetary Science Letters, v. 114, p. 193–209.

Stelten, M.E., Downs, D.T., Dietterich, H.R., Calvert, A.T., Sisson, T.W., Mahood, G.A., and Zahran, H., 2020, The timing and compositional evolution of volcanism within northern Harrat Rahat, Kingdom of Saudi Arabia: Geological Society of America Bulletin, v. 132, no. 7–8, p. 1381–1403, https://doi.org/10.1130/B35337.1.

Stelten, M.E., Downs, D.T., Champion, D.E., Dietterich, H.R., Calvert, A.T., Sisson, T.W., Mahood, G.A., and Zahran, H.M., 2023, Eruptive history of northern Harrat Rahat—Volume, timing, and composition of volcanism over the past 1.2 million years, chap. D *of* Sisson, T.W., Calvert, A.T., and Mooney, W.D., eds., Active volcanism on the Arabian Shield—Geology, volcanology, and geophysics of northern Harrat Rahat and vicinity, Kingdom of Saudi Arabia: U.S. Geological Survey Professional Paper 1862 [also released as Saudi Geological Survey Special Report SGS–SP–2021–1], 46 p., https://doi.org/10.3133/pp1862D.

Stoeser, D.B., and Frost, C.D., 2006, Nd, Pb, Sr and O isotopic characterization of Saudi Arabian shield terranes: Chemical Geology, v. 226, p. 163–188.

Stracke, A., and Bourdon, B., 2009, The importance of melt extraction for tracing mantle heterogeneity: Geochimica et Cosmochimica Acta, v. 73, p. 218–238.

Stracke, A., Hofmann, A.W., and Hart, S.R., 2005, FOZO, HIMU and the rest of the mantle zoo: Geochemistry, Geophysics, Geosystems, v. 6, no. 5, 20 p., https://doi.org/10.1029/2004GC000824.

Stracke, A., Zindler, A., Salters, V.J.M., McKenzie, D., Blichert-Toft, J., Albarède, F., and Grönvold, K., 2003, Theistareykir revisited: Geochemistry, Geophysics, Geosystems, v. 4, no. 2, 49 p., https://doi.org/10.1029/2001GC000201.

Tiepolo, M., Oberti, R., Zanetti, A., Vannucchi, R., and Foley, S.F., 2007, Trace-element partitioning between amphibole and silicate melt: Reviews in Mineralogy and Geochemistry, v. 67, p. 417–452.

Till, C.B., Grove, T.L., and Krawczynski, M.J., 2012, A melting model for variably depleted and enriched lherzolite in the plagioclase and spinel stability fields: Journal of Geophysical Research, v. 117, no. B06206, https://doi.org/10.1029/2011JB009044.

Vervoort, J.D., Patchett, P.J., Blichert-Toft, J., and Albarède, F., 1999, Relationships between Lu-Hf and Sm-Nd isotopic systems in the global sedimentary system: Earth and Planetary Science Letters, v. 168, p. 79–99.

White, W.M., and Klein, E.M., 2014, The composition of the oceanic crust, chap. 4.13 *of* Treatise on Geochemistry (2d ed.): Elsevier, v. 4, p. 457–496.

Yang, H.J., Frey, F.A., Rhodes, J.M., and Garcia, M.O., 1996, Evolution of Mauna Kea volcano—Inferences from lava compositions recovered in the Hawaiian Scientific Drilling Project: Journal of Geophysical Research, v. 101, p. 11747–11768.

Yao, Z., Mooney, W.D., Zahran, H.M., and Youssef, S.E., 2017, Upper mantle velocity structure beneath the Arabian shield from Rayleigh surface wave tomography and its implications: Journal of Geophysical Research, v. 122, p. 6552–6568.

Moffett Field Publishing Service Center, California
Manuscript approved August 26, 2021
Edited by Monica Erdman
Layout and design by Kimber Petersen

USGS

Salters and others—**Isotopic and Geochemical Evidence for the Source of Volcanism at Harrat Rahat**—Professional Paper 1862–J

ISSN 1044-9612 (print)
ISSN 2330-7102 (online)
https://doi.org/10.3133/pp1862J